The GN Model of Non-Linear Propagation in Uncompensated Coherent Optical Systems

The GN Model of Non-Linear Propagation in Uncompensated Coherent Optical Systems

Pierluigi Poggiolini, *member, IEEE*

***Abstract*—This paper is devoted to an in-depth discussion of the Gaussian Noise (GN) model which describes non-linear propagation in uncompensated coherent transmission systems. Similar models and validation efforts are reviewed. Then, the main equations of the GN model are introduced. An intuitive physical interpretation of the equations and their features is proposed. The main characteristics of the non-linear interference (NLI) noise spectra that the GN model produces are discussed. To ease model exploitation, a new formulation in hyperbolic coordinates is proposed, which makes numerical integration faster. New approximate closed-form solutions are also provided. An extension of the GN model to distributed-amplification scenarios is introduced. NLI noise accumulation vs. distance and bandwidth are studied in depth. Finally, the GN model implications as to system and networks design and optimization are discussed.**

***Index Terms*—coherent systems, non-linear effects, uncompensated transmission, GN model**

I. Introduction

THE dramatic revolution in optical transmission systems, brought about by the introduction of coherent technologies, has been multi-faceted. One of its many aspects involves the possibility of completely removing dispersion compensation from the link. Besides being beneficial in various practical ways, uncompensated transmission (UT) has also drastically changed the key features of signal propagation and of non-linearity generation in the fiber. In fact, as a further unexpected advantage from coherent technology, in the novel UT propagation regime it appears to be possible to carry out system performance prediction based on relatively simple analytical non-linear propagation models. These models appear to have a rather good predictive power and could substantially ease the analysis and design of optical systems and networks.

Most models for UT proposed so far are perturbative ones, i.e., they assume that non-linearity is relatively small vs. the useful signal. Also, a common feature is the assumption that non-linearity disturbance, which will be called non-linear interference (NLI) in this paper, manifests itself as additive Gaussian noise. Moreover, they appear to rely directly or indirectly on the circumstance, specific to UT, that the signal itself becomes indistinguishable from Gaussian noise due to the unmitigated effect of dispersion.

At a close look, many of these models, some of which were originally proposed many years ago, appear to show a high degree of convergence among them. They are briefly reviewed in the next section. This paper focuses on one specific instance of this class of models, which was called 'Gaussian Noise (GN) model' in [1] because of the relevance in the model of the Gaussian noise features recalled above.

In general, the modeling effort is far from over and in fact, while this paper was being finalized, at least two new models have achieved publication. This is a positive process and certainly the next few years will see continuous improvements and refinements, based perhaps on different and varied modeling approaches. The GN model, however, with some limitations that will be addressed in the next section, appears to already have fairly accurate predictive power, as both simulations and preliminary experiments attest (see Sect. II-A). In a way, it could therefore become a benchmark for future models, to gauge the improvement they bring about.

This paper is devoted to an in-depth discussion of the GN model. It addresses previously published results which, in many cases, are extended and further developed. Original material is also proposed. The main goals of the paper are the following: first, making the GN model more intuitively understandable; second, making it more easily exploitable, both analytically and numerically; third: extending it to more general system scenarios, such as distributed amplification, and fourth, discussing its far-reaching implications as to system and networks design and optimization. Certain details and derivations are confined within appendices, for ease of readability.

II. Perturbative Non-Linearity Models

A review of various perturbative non-linearity models was recently proposed in [1]. There, this model class was essentially linked to two main perturbative derivation approaches: Volterra Series (VS) and Four-Wave-Mixing (FWM).

The VS approach dates back to 1997 [2] and consists of finding an approximate solution of the non-linear Schroedinger equation (NLSE) in terms of a truncated Volterra series, in frequency domain. In 2002 the approach was used to derive an actual power spectral density (PSD) of NLI, viewed as

Pierluigi Poggiolini is with Dipartimento di Elettronica e Telecomunicazioni, Politecnico di Torino, Corso Duca degli Abruzzi 24, 10129, Torino, Italy (pierluigi.poggiolini@polito.it).

This paper has been published by IEEE with the following Digital Object Identifier 10.1109/JLT.2012.2217729

An erratum has also been published as Digital Object Identifier 10.1109/JLT.2012.2237115 and its contents were included in this posted version.

Gaussian additive noise [3], from which non-linear capacity formulas were later obtained [4]. Notably, Eq. (10) in [3] is quite similar to the GN model equation adopted in this paper, Eq. (1).

The FWM-like models are based on ideally slicing up the signal spectrum into spectral components, whose non-linear beating during propagation is then analytically expressed in a fashion similar to the classical formulas of FWM. Based on the FWM approach, already in 1993 [5] a PSD of NLI had been derived, similar to the GN model equation, which was then taken up again in [6].

A third related approach makes use of time-domain VS [7], though limited to intra-channel non-linearity. The analytical formulas shown there appear distant from those of the GN model but, in a follow-up paper [8], an approximate relation similar to Eq. (14) of this paper is shown. Therefore, remarkably, even such time-domain approach shows convergence with the GN and the other models.

The interesting question arises of why the above models, developed many years ago, did not enjoy widespread adoption when originally published. The answer seems to be that they could not accurately model the dispersion-managed systems of the time. UT systems instead comply well with the key underlying assumptions of such models, making their predictions more reliable.

The FWM approach has been recently taken up again and carried to a high degree of refinement in the context of OFDM [9]-[11]. A similar effort was made in parallel, aimed at generic WDM systems [12]. The reference Eq. (1) used here is taken from [1], a follow-up paper of [12].

While this paper was being finalized, further models have appeared, such as [13]–[14]. While they are too recent to comment upon, they show that substantial efforts are ongoing towards developing alternative and improved models.

A. Validation and limitations

Recent experiments have provided compelling evidence [15], confirming prior simulative results [16], that suggests that NLI noise is approximately Gaussian and additive. This is one of the main pillars of the GN model and its confirmation is of great significance.

The GN model quantitative predictions have been tested in [1] and [12] by means of a thorough simulation campaign, encompassing four different coherent formats, three fiber types, and different channel spacings. In all cases, the GN model proved quite accurate in predicting the system maximum reach, to within a few percent of error. However, such validations were carried out mostly at 32 GBaud, with relatively few data points obtained at lower symbol rates. Hence, the reliability of the model at lower symbol rates, such as 10-12 GBaud, still needs to be confirmed.

A preliminary experimental validation was carried out in [17] using a 10-channel 30 GBaud polarization-multiplexed quadrature phase-shift-keying (PM-QPSK) system with narrow spacing (33 GHz), tested over three fiber types. The GN model led to rather accurate predictions of system performance.

Other experiments have been lately conducted, aimed at studying the accumulation of NLI noise over distance [15], [18]–[19]. Some of the results seem to be compatible with the GN model predictions, while others are not. On the other hand, there appears to be disagreement even among results regarding similar system set-ups and therefore further investigation is needed before conclusions can be drawn. NLI accumulation will be specifically addressed in Sect. IX.

One known limitation of the GN model, observed but not yet thoroughly studied, depends on the underlying assumption that the signal is essentially Gaussian noise itself. This is very well verified provided that accumulated dispersion and symbol rate are large enough. In a typical 30 GBaud system over SMF, such condition is approximately reached after 200km. However, at low symbol rate or over NZDSF, it may take several spans for the signal to fully 'gaussianize'. This also means that using the GN model to predict the performance of single-span systems may lead to inaccurate predictions. Signal 'gaussianization' and its impact on model accuracy are currently under investigation. Another aspect currently under investigation is whether the model accuracy changes according to the number of WDM channels and specifically whether it is reliable for modeling single-channel transmission.

Nonetheless, the accumulated evidence so far hints at the GN model producing reliable predictions for symbol rates $\geq$ 28 GBaud, for channel spacings up to 100 GHz, of systems of at least 3 channels, over fibers with $D \geq$2 ps/(nm $\cdot$ km) and over more than a single span. Within these boundaries, the impact of the initial gaussianization of the signal appears to be minor. Also, experimental results at 14 GBaud with PM-16QAM (Quadrature-Amplitude-Modulation) over large-effective-area pure-silica-core fiber (PSCF) delivered results quite close to the model predictions [19]. Substantial research is underway to explore the model validity at lower symbol rates, lower dispersion values and for single-channel transmission, and to quantitatively estimate any error due to the initial non-gaussianity of the signal.

So far, GN-model-specific validation efforts have been carried out assuming systems with identical spans. In practical systems there may be a mixture of different spans, using different fibers. In [20] it was shown that system performance may depend on the ordering of fibers, especially when high and low dispersion fibers are involved. This paper is devoted to an in-depth study of the GN model features and predictions in the context of identical-span systems and therefore mixed-fiber links will not be addressed. However, it is important to point out that this aspect needs further study and perhaps specific model extensions to properly deal with it.

In summary, the GN model validation tests conducted so far have been rather positive. However, there is clearly the need for further extensive tests and studies in order to confirm these findings and to fully understand the limits of validity of the GN model.

III. The GN Model Reference Formula

In this section, the GN model main formula is introduced. An intuitive physical explanation of the phenomena it describes is proposed.

Some of the symbols that appear below are defined and listed here for convenience:

- α: fiber loss coefficient [km^{-1}], such that signal *power* is attenuated over a span as $\exp(-2\alpha L_s)$
- β_2: absolute value (always positive) of dispersion in [ps^{2}km^{-1}]
- γ: fiber non-linearity coefficient [W^{-1}km^{-1}]
- L_s: span length [km]
- L_{eff}: effective length [km], defined as $[1-\exp(-2\alpha L_s)]/2\alpha$
- N_s: number of spans

The GN model equation shown here is derived from Eq. (18) of [1]. It has been slightly modified to ease its physical interpretation:

$$G_{\text{NLI}}(f) = \tfrac{16}{27}\gamma^2 L_{\text{eff}}^2 \cdot \int_{-\infty}^{\infty}\int_{-\infty}^{\infty} G_{\text{WDM}}(f_1)\, G_{\text{WDM}}(f_2)\, G_{\text{WDM}}(f_1+f_2-f) \cdot \rho(f_1,f_2,f)\cdot\chi(f_1,f_2,f)\; df_2\, df_1 \,. \quad (1)$$

This equation will be called 'GNRF' (GN model Reference Formula). It represents the power spectral density of NLI noise at the end of a link. It assumes that all spans in the link are identical and that the loss of each span, including the last one, is exactly compensated for by optical amplification.

As shown in [1], the GNRF is derived by first inserting into the Manakov equation a WDM Tx signal modeled as a suitable Gaussian random process whose spectrum is composed of arbitrarily many spectral lines; then, using perturbative techniques and proper ensemble averaging, the final result Eq. (1) is found. A document providing more details on the derivation steps outlined in [1] is also available [26].

The GN-model can handle links with arbitrarily different spans [26]. This paper focuses on identical spans because this case makes it easier to discuss the key features of NLI.

The GNRF can be physically interpreted as describing the beating of each thin spectral slice of the WDM signal with all others through a FWM process. This is reflected in the presence within the double integral of the GNRF of a factor which represents the normalized FWM efficiency $\rho(f_1,f_2,f)$ of the beating of three 'pump' frequencies f_1, f_2 and $f_3 = (f_1+f_2-f)$ [21], creating an interfering signal at frequency f. Assuming lumped (EDFA) amplification:

$$\rho(f_1,f_2,f) = \left|\frac{1-e^{-2\alpha L_s}e^{j4\pi^2\beta_2 L_s(f_1-f)(f_2-f)}}{2\alpha - j4\pi^2\beta_2(f_1-f)(f_2-f)}\right|^2 \cdot L_{\text{eff}}^{-2} \quad (2)$$

where L_{eff} is used to normalize the maximum of ρ to 1. Note that the third 'pump' frequency f_3 does not explicitly appear in the GNRF, since it is implied by the physical constraint $f_3 = f_1+f_2-f$. In Sect. X a more general definition of ρ will be provided to encompass arbitrarily distributed amplification as well. For convenience, lumped amplification will be assumed in all other sections, unless otherwise specified.

The integrand factor:

$$G_{\text{WDM}}(f_1)G_{\text{WDM}}(f_2)G_{\text{WDM}}(f_1+f_2-f)$$

represents the power spectral density, i.e., the 'strength', that each of the three pumps carries. Finally, the factor:

$$\chi(f_1,f_2,f) = \frac{\sin^2\left(2N_s\pi^2(f_1-f)(f_2-f)\beta_2 L_s\right)}{\sin^2\left(2\pi^2(f_1-f)(f_2-f)\beta_2 L_s\right)} \quad (3)$$

takes into account the coherent interference at the receiver location of the NLI produced in each span. Hence, it governs NLI accumulation along the link. χ is sometimes called 'phased-array factor' since it is formally identical to the equation of the radiation pattern of a phased-array antenna. Such interference effect, with a similar analytical form, was pointed out in the context of conventional FWM calculations [21], [22] and discussed in detail in [9] in the context of OFDM systems. Noise accumulation is quite important and will be dealt with in depth in Sect. IX.

Finally, it should be recalled that according to the assumption that NLI is Gaussian and additive, system performance is governed by a modified OSNR which includes both ASE and non-linear noise contributions as follows:

$$\text{OSNR}_{\text{tot}} = \frac{P_{\text{ch}}}{P_{\text{ASE}}+P_{\text{NLI}}} \quad (4)$$

where P_{ch} is the launched power per channel and P_{ASE}, P_{NLI} are the ASE and NLI noise powers falling within the chosen OSNR conventional noise bandwidth B_N. The link between the NLI noise PSD provided by the GNRF and P_{NLI} in Eq. (4) is discussed in detail in Sect. XII.

IV. The reference system configurations

Throughout the following, various system configurations will be used as reference study cases. They are based on three fiber types, whose parameters approximately correspond to SMF, NZDSF and modern large-effective-area PSCF (see Table I). The latter will be called 'LPSCF' for short. Note that the dispersion parameter β_2 listed in the previous section is related to D in Table I as follows: $\beta_2 = |D|\cdot\lambda^2/(2\pi\cdot c)$, where c is the speed of light and λ is the operating wavelength.

The span length is set at L_s=100 km. The channel spacing is assumed to be Δf=50 GHz and the symbol rate is set at R_s=32 GBaud. Channel spectra are assumed to have a raised-cosine shape with roll-off equal to 0.3. The resulting full channel bandwidth, null-to-null, is hence 41.6 GHz. The number of channels N_{ch} is assumed to be such as to saturate the full C-band (unless otherwise specified), whose spectral extension is approximately 5 THz, according to the most current definitions. In order to have a 'center channel' in the comb, an odd number of channels was chosen: N_{ch}=101. These parameters were selected because they are approximately aligned with the current state-of-the-art of optical systems. The three reference systems will be referred to as 'RS' followed by the fiber acronym (for instance: RS-SMF).

In addition to these three systems, another set of three systems will be used, which assume ideal 'Nyquist WDM' transmission. This means that the channel spectra are assumed to be perfectly rectangular with bandwidth equal to the symbol rate. Also their spacing is assumed to be equal to the symbol rate, so that such systems are characterized by an overall rectangular signal spectrum $G_{\text{WDM}}(f)$ of full extension

Fiber	α [dB/km]	D [ps/nm/km]	γ [1/W/km]
LPSCF	0.165	20.4	0.8
SMF	0.2	16.5	1.3
NZDSF	0.2	3.9	1.6

TABLE I
PARAMETERS OF THE THREE FIBER TYPES USED AS REFERENCE THROUGHOUT THE PAPER.

$B_{\rm WDM} = N_{\rm ch} \cdot R_s$. A value $N_{\rm ch}$=157 is chosen, resulting again in $B_{\rm WDM} \approx 5$ THz. These systems will be identified by the acronyms NY-SMF, NY-NZDSF and NY-LPSCF.

The transmission format is left unspecified because the GN model shows no dependence on it. The format sets the system sensitivity in linearity and when this quantity is needed, proper mention of it will be made. Finally, the number of spans N_s will be specified case by case.

V. THE GNRF INTEGRATION DOMAIN

The GNRF requires that a double integration be carried out over the plane (f_1, f_2). The actual domain of this integration is limited because of the limited bandwidth of the transmission spectrum $G_{\rm WDM}$. In the following, the GNRF integration domain is studied in detail. This analysis will later be instrumental in finding effective numerical integration techniques and in deriving closed-form approximate solutions.

The WDM comb overall bandwidth will be called $B_{\rm WDM}$. It is then assumed for convenience that frequency f=0 corresponds to the center frequency of the WDM comb spectrum $G_{\rm WDM}(f)$. Note that, as a result, $G_{\rm WDM}(f)$=0 for $f > B_{\rm WDM}/2$ or $f < -B_{\rm WDM}/2$.

The evaluation of $G_{\rm NLI}(f)$ at f=0, that is at the center of the comb, is addressed first. In this case, the outer boundaries of the integration domain of the GNRF over the (f_1, f_2) plane are as depicted in Fig. 1. Note that it is possible to also draw the f_3 axis on the same plane, as shown, with the only caveat that it is not isometric with respect to the others, since $f_3 = f_1 + f_2$. In other words, given a certain geometric length d in the plot, which amounts to a frequency interval δf along either the f_1 or f_2 axes, it then amounts to a frequency interval $\sqrt{2} \cdot \delta f$ over the f_3 axis. The individual boundaries along either the f_1, f_2 or f_3 axes are induced by $G_{\rm WDM}(f_1)$, $G_{\rm WDM}(f_2)$ or $G_{\rm WDM}(f_1 + f_2)$ being zero, respectively. They are shown as thin dashed lines.

When the NLI PSD is evaluated at an arbitrary $f \neq$0, the f_1 and f_2 boundaries are not affected, since the factors $G_{\rm WDM}(f_1)$, $G_{\rm WDM}(f_2)$ do not contain f in their arguments. Instead, the third WDM spectrum factor $G_{\rm WDM}(f_1 + f_2 - f)$ gets shifted, altering the domain. An example of this is shown in Fig. 2 for $f = -0.3 \cdot B_{\rm WDM}$. It can be seen that the two diagonal thin lines expressing the f_3 boundary are shifted downward by f.

So far, only the outer boundaries of the integration domain have been addressed. However, in general, such domain is not internally compact. Specifically, if the WDM channels are spectrally separate by guard bands devoid of signal, then the integration domain within its outer boundaries becomes a collection of 'islands'. Assuming for convenience that the WDM comb consists of an odd number of channels, whose individual

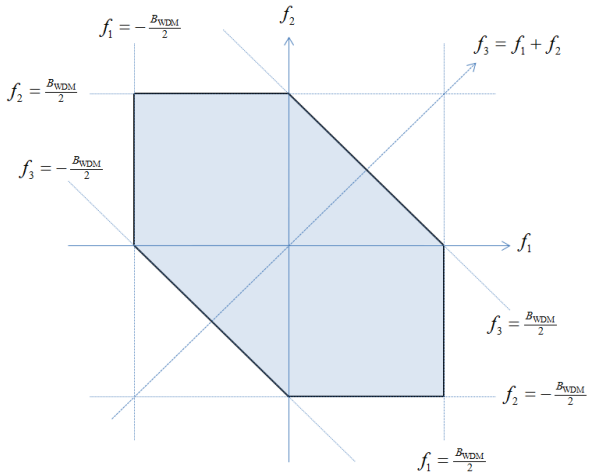

Fig. 1. Outer boundaries of the integration domain of the GNRF, delivering $G_{\rm NLI}(f)$ at a frequency f=0. Such frequency corresponds to the center frequency of the transmitted signal spectrum. The quantity $B_{\rm WDM}$ is the WDM comb overall optical bandwidth.

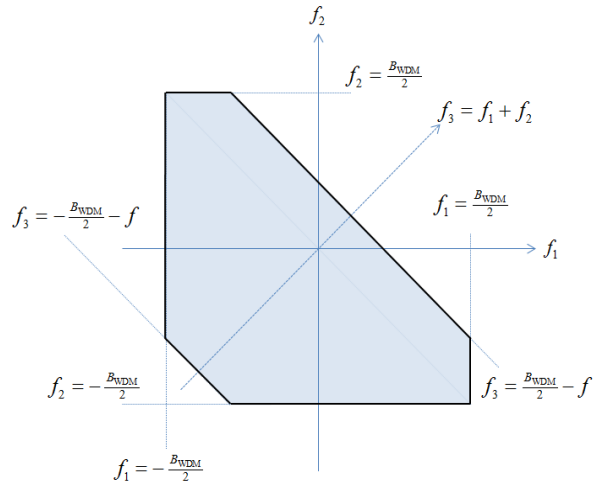

Fig. 2. Example of the outer boundaries of the integration domain of the GNRF, delivering $G_{\rm NLI}(f)$ at a frequency $f \neq$0. In the plot, $f = -0.3 \cdot B_{\rm WDM}$. The quantity $B_{\rm WDM}$ is the WDM comb overall optical bandwidth.

spectrum is symmetric with respect to their respective carriers, with uniform frequency spacing Δf and identical individual bandwidth $B_{\rm ch} \leq \frac{2}{3}\Delta f$, then the integration domain delivering $G_{\rm NLI}(f)$ at f=0 shapes up as in Fig. 3, where the case of 7 channels is shown. Interestingly, each individual island in the plot bears exactly the same lozenge-like shape as the overall outer boundary.

When $B_{\rm ch} > \frac{2}{3}\Delta f$ then other islands appear, which complicate the picture, although qualitatively the situation remains similar. This case is dealt with in Appendix A. Finally, in the Nyquist-WDM case, that is when $B_{\rm ch} = \Delta f$, all islands disappear, the integration domain becomes compact and it looks like in Fig. 1. In the following, for the sake of clarity, when dealing with the non-Nyquist case, $B_{\rm ch} \leq \frac{2}{3}\Delta f$ will be assumed.

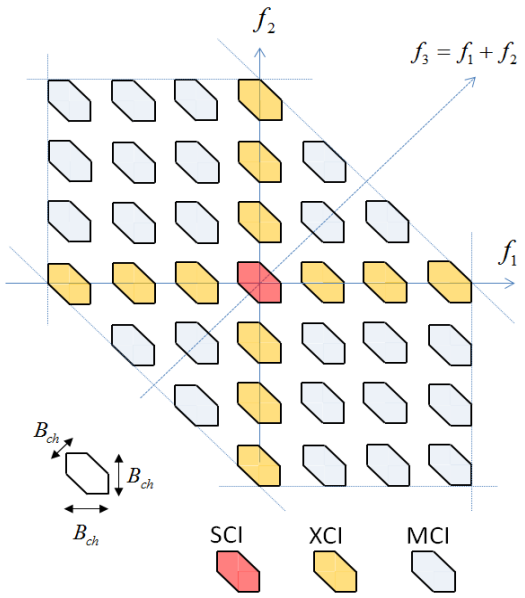

Fig. 3. Integration domain 'islands' of the GNRF, when the transmitted signal is made up of 7 equally-spaced identical channels with $B_{\rm ch} = \frac{2}{3}\Delta f$. The islands are classified according to the type of NLI they give rise to (see Sect. VI): SCI, self-channel interference; XCI: cross-channel interference; MCI, multi-channel interference.

The meaning of the plot of Fig. 3 is the following: given any point within any of the islands, the (f_1, f_2, f_3) coordinates of such point identify the three signal spectral components which are beating to create a NLI contribution at frequency f. Incidentally, this circumstance permits to propose a possible classification of the different islands in terms of non-linearity classes, as explained in the next section.

VI. Classifying Non-Linear Contributions

In the following, the focus will be on $G_{\rm NLI}(0)$, that is assuming $f = 0$. Generalizations are straightforward. Note that the classification below is precise and clear-cut as long as $B_{\rm ch} \leq \frac{2}{3}\Delta f$. Otherwise, it is still valid in general qualitative terms but the overall picture becomes more complex (see Appendix A).

1) Self-Channel Interference (SCI): The island sitting at the origin of Fig. 3 contains all points whose related frequencies (f_1, f_2, f_3) belong, all three, to the center channel and whose beating adds up at the center frequency of the same channel. Therefore, it seems reasonable to classify such constributions as 'self-channel interference', or SCI. An example of SCI is depicted in Fig. 4-a.

2) Cross-Channel Interference (XCI): The islands sitting across either the vertical or the horizontal axis in Fig. 3, except the one at the origin, contain all points whose related frequencies (f_1, f_2, f_3) are such that they belong to either the center channel or one, and only one, other channel. In other words, these contributions to $G_{\rm NLI}(0)$ involve an *interplay* between the center channel and *one* other channel. A possible terminology to denote them is then 'cross-channel interference' or XCI. An example of XCI is depicted in Fig. 4-b.

Note that the contribution of the islands along the vertical axis are exactly equivalent to those along the horizontal axis, so that they could be calculated only once, along either axis. This and other symmetries in the integration process are discussed in Sect. VIII.

3) Multi-Channel Interference (MCI): All other islands contain points whose related frequencies (f_1, f_2, f_3) are such that each triple involves at least two channels other than the center channel. The latter may or may not be involved.

Specifically, the islands that sit across the bi-sector of the II-IV quadrants are characterized by f_3 belonging to the center channel and by f_1 and f_2 always belonging to two other different channels. Apart from such islands, all others do not involve the center channel.

Since these contributions to $G_{\rm NLI}(0)$ involve more than two channels, namely three or even four, a possible appropriate terminology to denote them is 'multi-channel interference' or MCI. An example of MCI is depicted in Fig. 4-c.

A. On the relative strength of SCI, XCI and MCI

The three types of UT non-linearity have the same qualitative effect: adding Gaussian noise to the signal. However, they have a strikingly different quantitative system impact. Specifically, MCI is almost always negligible. In RS-NZDSF it accounts for less than 1% of the total $G_{\rm NLI}(0)$, for any number of spans. In RS-SMF and RS-LPSCF its impact is even smaller.

Regarding SCI and XCI, they are much more balanced and, depending on system parameters, either one can prevail. In particular, it is mainly the total number of channels or, equivalently, the overall system optical bandwidth $B_{\rm WDM}$ that sets their ratio. Dispersion also has an impact. This matter will be discussed in a specific section devoted to NLI noise accumulation versus $B_{\rm WDM}$ (Sect. IX-B). More details regarding the relative strength of the various regions of the (f_1, f_2) plane will also be provided in Sect. VIII, which is devoted to techniques for the efficient evaluation of the GNRF.

B. Comparison with prior non-linearity taxonomy

An interesting question is whether a correspondence can be found between the above NLI taxonomy for UT systems and the traditional taxonomy of dispersion-managed systems, that is SPM, XPM, XPolM. The answer appears to be in the negative.

First of all, the traditional effects have each a very specific way of impacting the signal, with peculiar features. Instead, all NLI effects in UT systems end up having the same qualitative effect of creating further additive Gaussian noise on top of the useful signal, uncorrelated with the signal itself.

Of course, one could be tempted to still call 'SPM' the NLI caused by a single channel onto itself, which here is termed instead 'SCI'. However, calling it 'SPM' would be quite misleading, since SCI does not at all manifest itself as 'self phase modulation'. Similar arguments can be used for XPM or XPolM with respect to both XCI and MCI.

In essence, there is little or no correspondence between UT systems with their Gaussian NLI and DM systems with their

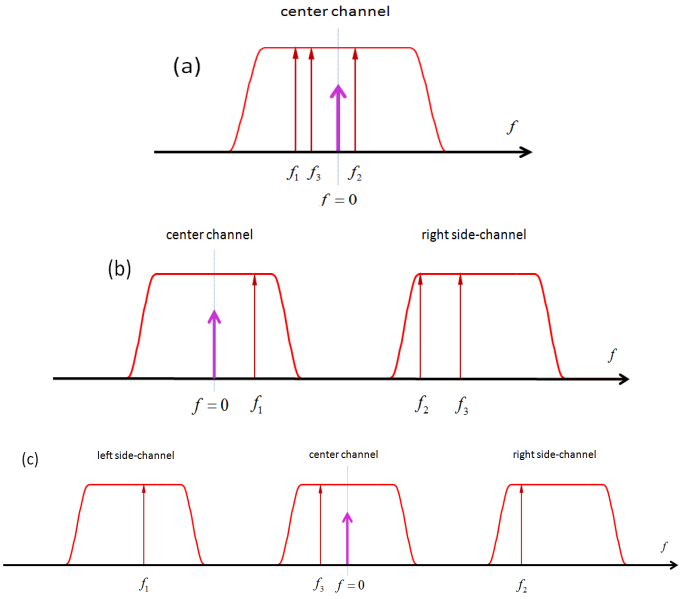

Fig. 4. Examples of NLI contributions according to the classification of Sect. VI. Thin tall arrows: generating signal components. Thick shorter arrows: generated NLI contributions. (a): SCI, self-channel interference; (b): XCI, cross-channel interference; (c): MCI, multi-channel interference.

structured non-linear effects. Therefore, the old taxonomy, with its implications, appears not to be applicable to UT systems.

VII. The shape of the NLI power spectral density

The shape of the NLI PSD $G_{\rm NLI}(f)$ is important in view of its use in assessing system performance. In particular, if $G_{\rm NLI}(f)$ turned out to be approximately flat over the bandwidth of any given WDM channel, then NLI noise could be considered Gaussian, additive and *locally white*. As a result, system performance calculations would be greatly eased.

In Fig. 5, $G_{\rm NLI}(f)$ is shown for the case of a NY-SMF system at N_s=20 spans, with overall optical bandwidth $B_{\rm WDM}$=544 GHz, equivalent to 17 Nyquist-WDM channels at 32 GBaud. The plot clearly shows that the PSD of NLI noise is relatively flat over all channels, with the exception of just the outermost ones. In particular, it is nearly perfectly flat over the center channel, which is also the most impacted.

In Fig. 6, top, a more conventional RS-SMF system is shown, with 11 channels, with a similar $B_{\rm WDM}$=541.6 GHz. Between channels, $G_{\rm NLI}(f)$ dips significantly. It also rolls-off somewhat over the spectral region occupied by each channel. As it could be expected, here too NLI noise peaks at the center frequency of the center channel, which is again the most impacted. A zoomed-in version of the same plot showing just the center channel is reported in Fig. 6, bottom. It can be appreciated how $G_{\rm NLI}(f)$ follows closely the shape of the signal spectrum, albeit with a somewhat enhanced roll-off.

In this case, assuming a receiver filter matched to the transmission signal spectrum, the NLI noise variance found after the filter when using the locally white approximation of NLI noise, i.e., a flat PSD equal to $G_{\rm NLI}(0)$, is less than 0.5 dB larger than the variance found when the actual NLI

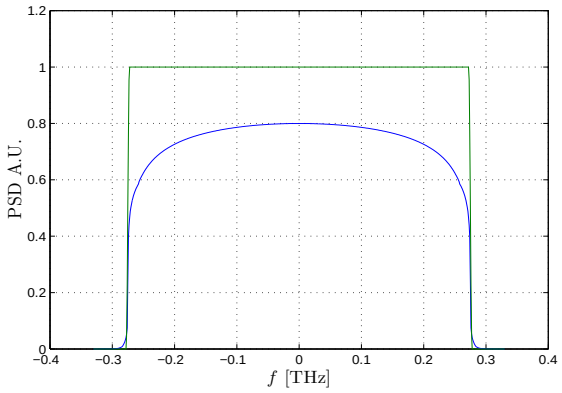

Fig. 5. NY-SMF system, with 20 spans. Green solid line: PSD of the transmitted signal $G_{\rm WDM}(f)$, equivalent to 17 Nyquist-WDM channels at 32 GBaud. Blue solid line: PSD of NLI noise $G_{\rm NLI}(f)$. Spectra arbitrarily rescaled for ease of comparison.

PSD is passed through the matched filter. In terms of system performance estimation, an error of this magnitude turns out to be of very limited impact: as it will be shown in Sect. XII-B, a 0.5 dB greater NLI noise causes only a 4% decrease in the system theoretical maximum reach prediction.

In addition, the locally white NLI assumption, with flat PSD value equal to that at the channel center frequency, is typically conservative for the center channel, that is it leads to a slightly pessimistic performance assessment. In many cases this accuracy can be good enough, otherwise it is relatively straightforward to improve the NLI noise variance estimate by evaluating the NLI PSD at a few other frequencies within the channel.

VIII. Evaluating the GNRF

Although some closed-form approximate solutions are available under certain assumptions (Sect. XI), in general the GNRF cannot be solved analytically. If approximations are not acceptable, there is no alternative to numerical integration. Unfortunately, a brute-force approach is not viable, as explained in Appendix B. In the following, an alternative form of the GNRF in hyperbolic coordinates is shown, which permits much faster numerical integration.

A. Hyperbolic coordinates

For simplicity, here it is assumed that the GNRF is evaluated at f=0 and that $G_{\rm WDM}$ is even, that is $G_{\rm WDM}(f)$=$G_{\rm WDM}(-f)$. Both assumptions can be removed, as shown in Appendix E.

Looking at both the ρ and χ integrand factors for f=0, it can be observed that they depend solely on the product $(f_1 f_2)$. Exploiting the $(f_1 f_2)$ dependence, it is possible to re-cast the GNRF in *hyperbolic* coordinates, defined as follows:

$$\begin{cases} \nu_1 = \sqrt{f_1 f_2} \\ \nu_2 = -\frac{1}{2}\log_e\left(\frac{f_2}{f_1}\right) \end{cases}, \quad \begin{cases} f_1 = \nu_1 e^{\nu_2} \\ f_2 = \nu_1 e^{-\nu_2} \end{cases}$$

The Jacobian is $2\,|\nu_1|$. Operating this substitution and taking advantage of the symmetries pointed out in Appendix C, the

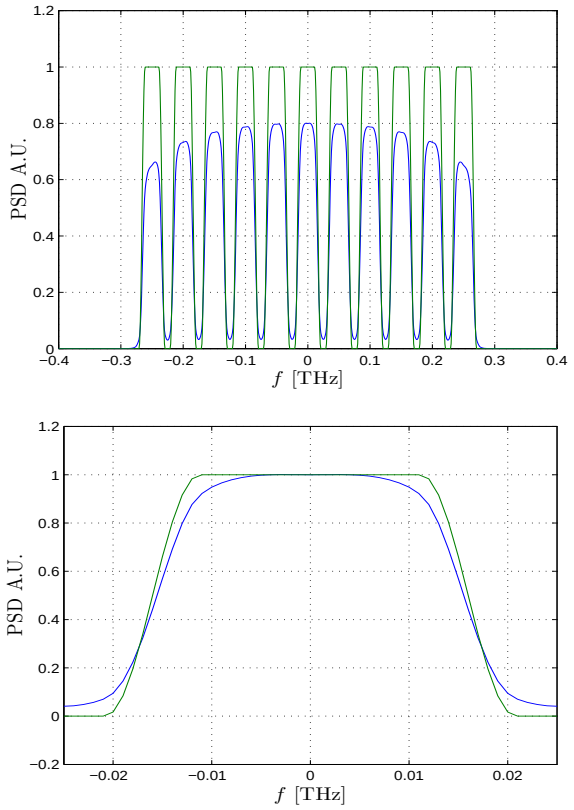

Fig. 6. RS-SMF system, with 20 spans. Top plot: green solid line: PSD of the transmitted signal $G_{\mathrm{WDM}}(f)$, equivalent to 11 channels at 32 GBaud; blue solid line: PSD of NLI noise $G_{\mathrm{NLI}}(f)$. Bottom plot, same as top, zoomed in on the center channel. Signal and NLI spectra arbitrarily rescaled in each plot for ease of comparison.

GNRF at f=0 can be re-written as:

$$G_{\mathrm{NLI}}(0) = \tfrac{64}{27}\gamma^2 N_s L_{\mathrm{eff}}^2 \int_0^{B_{\mathrm{WDM}}/2} \rho(\nu_1,0)\ \chi(\nu_1,0)\,|2\nu_1|\cdot \int_0^{\log_e(B_{\mathrm{WDM}}/2\nu_1)} G_{\mathrm{WDM}}(\nu_1 e^{\nu_2})\,G_{\mathrm{WDM}}(\nu_1 e^{-\nu_2})\cdot \cdot\left[G_{\mathrm{WDM}}\left(2\nu_1\cosh(\nu_2)\right)+G_{\mathrm{WDM}}\left(2\nu_1\sinh(\nu_2)\right)\right]\mathrm{d}\nu_2\mathrm{d}\nu_1 \tag{5}$$

where:

$$\rho(\nu_1,0) = \left|\frac{1-e^{-2\alpha L_s}e^{j4\pi^2\beta_2 L_s\nu_1^2}}{2\alpha-j4\pi^2\beta_2\nu_1^2}\right|^2\cdot L_{\mathrm{eff}}^{-2}$$
$$\chi(\nu_1,0) = \frac{\sin^2\left(2N_s\pi^2\nu_1^2\beta_2 L_s\right)}{\sin^2\left(2\pi^2\nu_1^2\beta_2 L_s\right)} \tag{6}$$

All the details of the derivation are provided in Appendix E.

This formula in hyperbolic coordinates has three substantial advantages vs. the one in conventional coordinates. First, the highly peaky and oscillatory factor χ discussed in Appendix B depends only on ν_1 and therefore it is confined within one integral. While the double-integration of χ is daunting, its single-dimension integration is doable. Secondly, the inner integral over ν_2 contains only the WDM signal spectrum factors and this integrand is typically well-behaved.

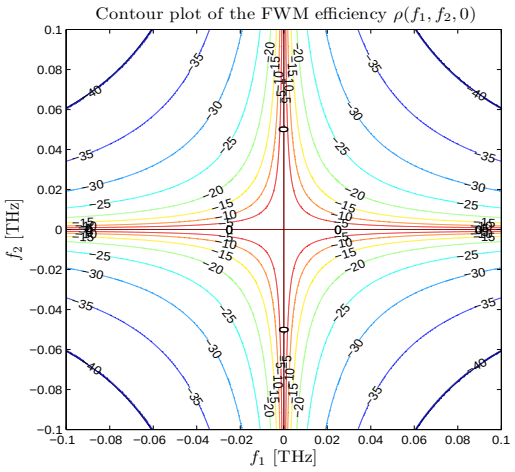

Fig. 7. Contour plot in dB of the FWM efficiency factor $\rho(f_1, f_2, 0)$, present in the integrand of the GNRF, shown for SMF in the domain $f_1, f_2 \in [-0.1, 0.1]$ THz. In hyperbolic coordinates, each contour line corresponds to a single value of ν_1, where ρ is a constant.

Finally, and perhaps most important, integration can typically be stopped well before the full range $[0, B_{\mathrm{WDM}}/2]$ has been spanned by ν_1, exploiting the fast decay of $\rho(\nu_1, 0)$ vs. increasing ν_1. In fact, each value of ν_1 univocally identifies a hyperbole in the (f_1, f_2) plane, such as those shown in Fig. 7, where the FWM efficiency $\rho(\nu_1, 0)$ has the same value. Note that increasing ν_1 means moving outward from one contour line to the next in Fig. 7. This suggests that one could limit the integration range along ν_1 to cut off the outer regions in Fig. 7 where ρ has uniformly decayed below a certain very low level, say, -30 or -40 dB. An example of a curtailed integration domain is the one comprised within the four hyperboles depicted in Fig. 8. In that case, the resulting relative error in the evaluation of $G_{\mathrm{NLI}}(0)$ for a RS-SMF with B_{WDM}=5 THz is less than 10^{-4}. More details on this aspect can be found in Appendix D. Incidentally, Fig. 7 shows why SCI and XCI contributions are typically prevailing. An analytical estimate of the error incurred in curtailing ν_1 is also available and is reported in Appendix D-A.

To ease integration, further manipulation of Eq. (5) is possible, as commented in Appendix E-B. In summary, operating in hyperbolic coordinates greatly reduces the complexity of the numerical integration of the GNRF. Using Eq. (5), it is found that full C-band accurate integration of the GNRF is possible within reasonable CPU times. As an example, $G_{\mathrm{NLI}}(0)$ was calculated for a C-band RS-SMF system, at each number of spans N_s from 1 to 100. Interpreted Matlab$^{\mathrm{TM}}$ code was used, with integration settings capable of ensuring a relative error of less than $5\cdot 10^{-3}$. In total, the calculation took 300 seconds, an average of 3 s per value.

IX. NLI Noise Accumulation

A key question related to the overall GN model is what kind of NLI noise accumulation occurs vs. optical signal bandwidth B_{WDM}, or number of channels N_{ch}, and vs. number of spans N_s.

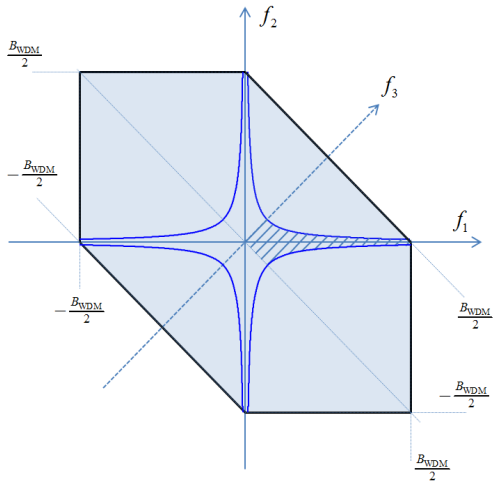

Fig. 8. Example of curtailed hyperbolic integration domain, represented by the region of the plane comprised within the four hyperboles. Due to symmetries, actual integration in Eq. (5) is performed only in the shaded region, with the result multiplied by four. The curtailing depicted in figure, if referred to RS-SMF with B_{WDM}=5 THz, would result in a relative error on the $G_{\mathrm{NLI}}(0)$ calculation of less than 10^{-4}.

Various experimental results are now available in the literature regarding accumulation vs. N_s, hinting at a law of the type:

$$G_{\mathrm{NLI}}(f) = G_{\mathrm{NLI}}(f)\,|_{N_s=1} \cdot N_s^{1+\epsilon} \tag{7}$$

The estimated values of ϵ range between 0 and 0.6 [15], [18]–[19]. Note that ϵ=0 means that the NLI produced in one span sums up in power, i.e., *incoherently*, with the contributions of all other spans. Instead, the closer ϵ is to 1, the greater is the coherence among NLI from different spans, with ϵ=1 corresponding to perfect phase-matching.

Fewer results are available on the dependence of NLI on the number of channels N_{ch} [28]. They hint at a non-negligible amount of NLI being generated even by channels that are far away from the one under test.

In the next sections, the issue of NLI accumulation is explored by looking at the predictions of the GN model, obtained through the accurate numerical integration of the GNRF, performed using Eq. (5). The procedure used to derive the results is the following. For each system scenario, $G_{\mathrm{NLI}}(0)$ is calculated for $N_{\mathrm{ch}} = 1 \ldots 101$ and for $N_s = 1 \ldots 100$. For the Nyquist-WDM case, instead of N_{ch} the parameter B_{WDM} is used, in the range 1 GHz to 5 THz. The resulting data is then post-processed to extract the relevant information.

An interesting aspect which emerges from the following analysis is that NLI accumulation vs. bandwidth and vs. distance are not independent, in the sense that noise accumulation vs. N_s depends on how large the optical signal bandwidth B_{WDM} is.

A. NLI accumulation vs. N_{s}

Fig. 9 shows the NLI accumulation curves vs. N_s for B_{WDM}= 0.2, 1 and 5 THz in the NY-SMF scenario. The plotted quantity is normalized as follows:

$$g_{\mathrm{NLI}}(N_s) = \frac{G_{\mathrm{NLI}}(0)\,|_{N_s}}{G_{\mathrm{NLI}}(0)\,|_{N_s=1}}$$

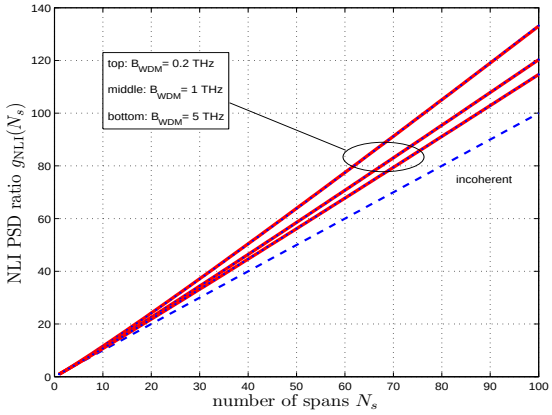

Fig. 9. Red solid lines: $g_{\mathrm{NLI}}(N_s)$, defined as the NLI noise PSD $G_{\mathrm{NLI}}(0)$ vs. number of spans N_s, relative to $G_{\mathrm{NLI}}(0)$ with N_s=1, for B_{WDM}= 0.2, 1 and 5 THz. Superimposed blue dots: best-fit according to Eq. (7). Bottom blue dashed line is incoherent accumulation, for comparison.

Qualitatively similar results are found for NY-LPSCF and NY-NZDSF. The solid curves are found through numerical integration of the GNRF and the dots are a best-fit according to Eq. (7). This plot shows that the simple exponential model of Eq. (7) is extremely effective in reproducing correctly NLI accumulation across the whole range of N_s. This is an important result, because it shows that such accumulation can be completely characterized through a single parameter ϵ, which is constant vs. N_s.

Fig. 10 shows the resulting best-fit values of ϵ for NY-SMF, NY-LPSCF and NY-NZDSF, vs. B_{WDM}. The plot shows qualitatively similar curves, with SMF and LPSCF almost coinciding. Notably, the terminal value for B_{WDM}=5 THz is almost the same for all curves, approximately $\epsilon \approx 0.035$. Also the initial value, for B_{WDM}=1 GHz, coincides at $\epsilon \approx 1$.

The latter value shows that NLI noise produced within 1 GHz of f=0 accumulates in a phase-matched way, span after span. The NLI field grows as N_s and so the NLI power grows as N_s^2. On the contrary, the NLI involving farther away frequencies is no longer phase-matched from one span to the next. When B_{WDM} is above 1 THz, ϵ gets below 0.05, which means that, overall, NLI accumulates almost incoherently. In practice, what happens is that NLI contributions originating far away from f=0 accumulate in a perfectly incoherent way; since they sum up with other contributions originated within a few GHz of f=0, which accumulate coherently, then the overall ϵ is a weighed average of these different regimes, with incoherent quantitatively prevailing and pulling ϵ towards 0.

For the non-Nyquist case, the exponential best-fit according to Eq. (7) turns out to be equally accurate and effective (plot not shown for brevity) as in the Nyquist-WDM case. Fig. 11 shows the best-fit values of ϵ for RS-SMF, RS-LPSCF and RS-NZDSF, vs. N_{ch}. Again, the plot shows qualitatively similar curves, with SMF and LPSCF almost coinciding. The terminal value is higher than in the Nyquist case, with $\epsilon \approx 0.06$ for SMF and LPSCF and about 0.07 for NZDSF. The slightly higher values of ϵ can tentatively be explained as follows. The SCI contribution, corresponding to N_{ch}=1

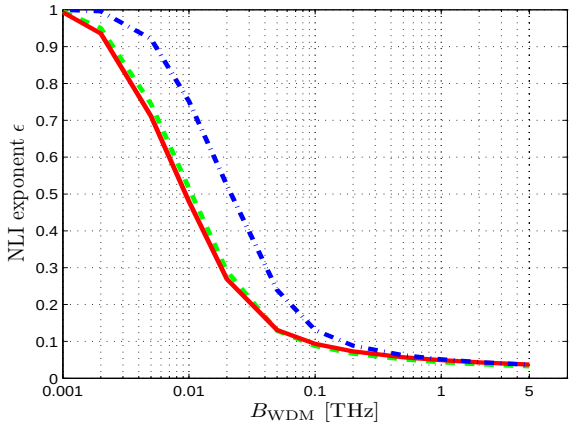

Fig. 10. NLI accumulation exponent ϵ, vs. optical signal bandwidth $B_{\rm WDM}$, with Nyquist-WDM signal. Red solid line: NY-LPSCF system; green dashed line: NY-SMF system; blue dash-dotted line: NY-NZDSF system.

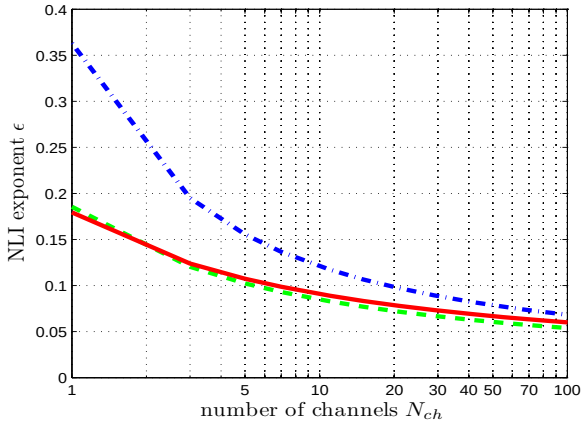

Fig. 11. NLI accumulation exponent ϵ, vs. number of channels $N_{\rm ch}$. Red solid line: RS-LPSCF system; green dashed line: RS-SMF system; blue dash-dotted line: RS-NZDSF system.

in the plot, has a relatively large ϵ: for SMF it is 0.19, for NZDSF it reaches 0.36. The remainder of the spectrum causes essentially incoherent accumulation, but there is less of it than in the Nyquist-WDM case because of the empty guard bands between channels. As a result, the overall ϵ is slightly higher than in the Nyquist WDM case.

If the channel spacing is increased to Δf=100 GHz, the values of ϵ tend to further increase, in agreement with the explanation given above. Their values at 51 channels (the whole C-band) are: RS-SMF 0.09; RS-LPSCF 0.096; RS-NZDSF 0.123. If instead the span length L_s is decreased to 50 km, while keeping Δf=50 GHz and $N_{\rm ch}$=101, then RS-SMF 0.088; RS-LPSCF 0.090; RS-NZDSF 0.103. In other words, both substantially increasing the channel spacing and decreasing the span length brings about a substantial increase in ϵ which, however, remains relatively small for C-band systems.

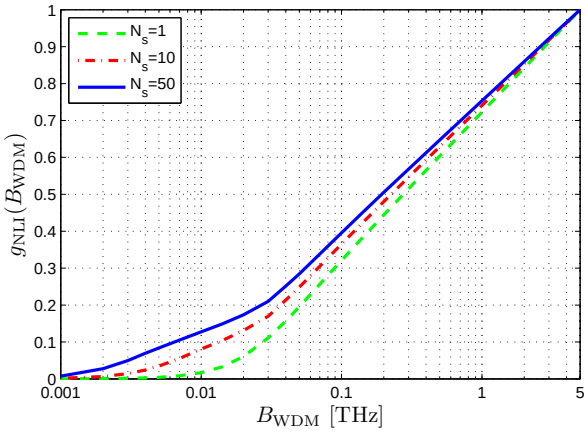

Fig. 12. Plot of $g_{\rm NLI}(B_{\rm WDM})$, defined as the NLI noise PSD $G_{\rm NLI}(0)$ vs. $B_{\rm WDM}$, relative to $G_{\rm NLI}(0)$ at $B_{\rm WDM}$=5 THz, for a NY-SMF system. In the legend, N_s is the number of spans.

B. NLI accumulation vs. $B_{\rm WDM}$

In Fig. 12 the results of NLI noise accumulation vs. optical signal bandwidth are shown for NY-SMF, as a function of $B_{\rm WDM}$. The plotted quantity is the ratio:

$$g_{\rm NLI}(B_{\rm WDM}) = \frac{G_{\rm NLI}(0)\,|_{B_{\rm WDM}}}{G_{\rm NLI}(0)\,|_{B_{\rm WDM}=5\,\rm THz}}$$

Three different curves, for N_s=1, 10 and 50 are shown. The interesting result is that NLI noise asymptotically grows according to a logarithmic law (straight line), with no sign of saturation.

The normalization of $g_{\rm NLI}$ allows to directly read off the bandwidth that corresponds to any fraction of the total C-band noise. For instance, for N_s=50 the plot shows that 50% of noise is produced by the first 200 GHz of signal spectrum alone, which also means that the remaining 50% is produced in conjunction with the outer 4.8 THz of signal spectrum.

Low bandwidths contribute more NLI noise when N_s is large because, as seen in the previous section, they have a higher ϵ, so their contribution to NLI gets more enhanced by a large N_s. This fact causes the 50% crossing bandwidth to shift towards lower values for increasing N_s.

In Fig. 13 results for RS-SMF are shown, as a function of $N_{\rm ch}$. The plotted quantity is the ratio:

$$g_{\rm NLI}(N_{\rm ch}) = \frac{G_{\rm NLI}(0)\,|_{N_{\rm ch}}}{G_{\rm NLI}(0)\,|_{N_{\rm ch}=101}}$$

Three different curves, for N_s=1, 10 and 50 are shown. Here too, NLI noise asymptotically grows according to a logarithmic law, with no sign of saturation. Again, $g_{\rm NLI}$ allows to directly read off the number of channels generating a certain fraction of the total C-band noise. For instance, 50% of noise is produced by the first 3, 5 and 6 channels for N_s=50, 10 and 1, respectively. Remarks similar to those proposed for the Nyquist-WDM case can be made here, regarding the curve hierarchy vs. N_s.

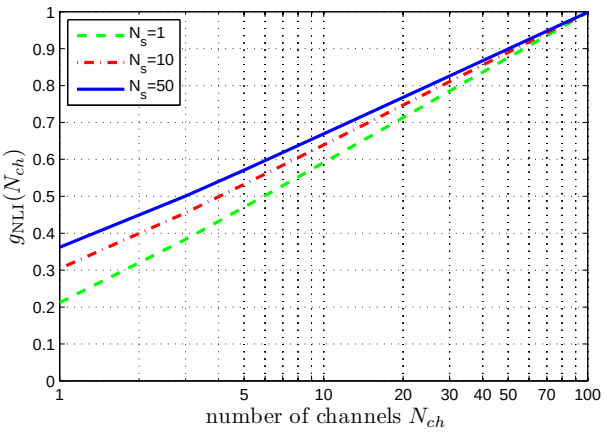

Fig. 13. Plot of $g_{\rm NLI}(N_{\rm ch})$, defined as the NLI noise PSD $G_{\rm NLI}(0)$ vs. the number of channels $N_{\rm ch}$, relative to $G_{\rm NLI}(0)$ at $N_{\rm ch}$=101, for a RS-SMF system. In the legend, N_s is the number of spans.

C. Comments on NLI accumulation

Because of space limitations, the above results explore only a limited set of scenarios. However, some conclusions can already be drawn regarding the GN model prediction on NLI accumulation.

Firstly, the simple exponential law given by Eq. (7) appears to be rather adequate to represent NLI growth vs. N_s in typical system scenarios.

Secondly, when a fully populated system, i.e., spanning the whole C band or greater, with standard 50 GHz spacing is considered, NLI accumulation vs. N_s is close to linear, that is, noise accumulates incoherently to a large extent. The typical value of the residual exponent ϵ is around 0.06, almost independently of the type of fiber used. Note though that, if the number of channels is small, especially with relatively large spacing, a substantially larger ϵ can be found.

Recent simulative results [27], as well as the experimental results reported in [19] and part of [18], appear to agree with such predictions on NLI accumulation vs. N_s. However, it must be pointed out that others do not, such as [15] and part of [18], which report higher values of ϵ than the GN model predicts. Clearly, more research and a careful comparison of analytical, simulative and experimental evidence is still necessary to settle the matter.

Thirdly, NLI noise appears to be generated even by far-away channels and in fact there is no channel far enough that it can be neglected. Specifically, XCI is responsible for the continued growth of NLI. A preliminary experimental confirmation of this trend is reported in [28].

This last aspect, if confirmed by further experiments, could have important implications. Specifically, the plots of Figs. 12 and 13 could be read as the fraction of NLI noise that could theoretically be compensated for by a receiver whose optical bandwidth corresponds to the abscissa of the plots, provided that such receiver is equipped with an ideal digital-signal-processing (DSP) non-linearity compensation algorithm.

To exemplify: Fig. 13 shows that in the RS-SMF case with 50 spans, 50% of the NLI noise on the center channel is produced by the center channel together with its two neighbors (3 channels in all). This means that to reduce $P_{\rm NLI}$ on the center channel by 50 % (3 dB), the receiver would need to have an optical bandwidth wide enough to ensure complete visibility of all three channels simultaneously (about 132 GHz). Unfortunately, as it will be shown in Sect. XII-B, a 3-dB reduction of $P_{\rm NLI}$ only gains 1 dB of system length increase (25%). To achieve more substantial gains, according to Fig. 13, dauntingly large receiver bandwidths and related DSP processing powers would be required. These results indicate that electronic non-linearity mitigation may face very challenging practical implementation hurdles.

X. Extending the GNRF scope

The $G_{\rm NLI}$ reference formula of Eq. (1) has two important limitations. One is that it can handle only lumped amplification. The other is that it addresses only systems with identical spans. The latter limitation can be removed as shown in [26] and will not be dealt with here. The next sections concentrate instead on removing the former.

A. A generalized $G_{\rm NLI}$ formula for arbitrary gain profiles

The specific form taken on by ρ in the GNRF depends on the underlying assumptions on loss and amplification. If a generic field loss $\alpha(z)$ and field gain profile $g(z)$ are assumed, then ρ can be calculated based on its general definition:

$$\rho\left(f_1,f_2,f\right)=\left|\int_0^{L_s} e^{-2\int_0^z\left[\alpha(z')-g(z')\right]dz'} e^{j4\pi^2\beta_2(f_1-f)(f_2-f)z}\,dz\right|^2\cdot L_{\rm eff}^{-2} \tag{8}$$

with:

$$L_{\rm eff}^2=\left|\int_0^{L_s} e^{-2\int_0^z\left[\alpha(z')-g(z')\right]dz'}\,dz\right|^2 \tag{9}$$

It is easy to see that by imposing: $\alpha(z)=\alpha$ and $g(z)=0$, then Eqs. (8)-(9) yield Eq. (2).

This general formulation of ρ is quite powerful as it permits to extend Eq. (1) to any arbitrarily distributed loss/gain profile, such as it could be produced for instance by a forward/backward-pumped Raman amplifier. Also, with straightforward manipulations, it can be inserted within the hyperbolic-coordinate versions of the GNRF given by Eqs. (5) and (35) for effective numerical integration.

In a few special cases, besides lumped amplification, it is possible to obtain ρ analytically. Two such cases are the standard backward-pumped Raman amplification, of great practical importance, and ideal loss-suppressing distributed amplification. The latter is significant for the assessment of the ultimate performance of distributed amplification.

B. Ideal loss-suppressing distributed amplification

If one assumes constant loss and also constant gain with $g(z)=\alpha$, then:

$$L_{\rm eff}^2\cdot\rho\left(f_1,f_2,f\right)=\left|\frac{\sin\left(2\pi^2\beta_2(f_1-f)(f_2-f)L_s\right)}{2\pi^2\beta_2(f_1-f)(f_2-f)L_s}\right|^2 \tag{10}$$

When this formula is inserted into the GNRF, a closed-form approximate analytical solution can be found for the Nyquist-WDM case, which is shown in Sect. XI-E.

For convenience, the formula for ASE noise from ideal distributed amplification is provided in Appendix J, which is needed when estimating $\mathrm{OSNR}_{\mathrm{tot}}$.

C. Backward-pumped Raman amplification

An analytical expression of ρ can be written for the case of a single Raman pump, with no pump depletion. If so, the Raman gain coefficient can be written as:

$$2g(z) = C_R P_{p_0} e^{2\alpha_p z} \tag{11}$$

where P_{p_0} is the pump power at the beginning of the span, which corresponds to an injected pump power at the span end equal to $P_p = P_{p_0} e^{2\alpha_p L_s}$. The constant α_p is the pump loss coefficient, which is in general different from the signal loss coefficient α, while C_R is the Raman gain constant, typically expressed as [1/(W·km)]. Then, the span FWM efficiency can be written as:

$$\begin{aligned} &L_{\mathrm{eff}}^2 \cdot \rho\left(f_1, f_2, f\right) = \\ &\left| \int_0^{L_s} e^{-2\alpha z} e^{C_R P_{p_0} \frac{e^{2\alpha_p z}-1}{2\alpha_p}} e^{j4\pi^2\beta_2(f_1-f)(f_2-f)z} dz \right|^2 = \\ &\left| \frac{e^{-C_R P_{p_0}/2\alpha_p}}{2\alpha_p} \left(-\frac{C_R P_{p_0}}{2\alpha_p}\right)^{\left[\frac{\alpha}{\alpha_p} - \frac{j2\pi^2\beta_2(f_1-f)(f_2-f)}{\alpha_p}\right]} \right. \\ &\left[\Gamma\left(-\left[\frac{\alpha}{\alpha_p} - \frac{j2\pi^2\beta_2(f_1-f)(f_2-f)}{\alpha_p}\right], -\frac{C_R P_{p_0}}{2\alpha_p}\right)\right. \\ &\left.\left. -\Gamma\left(-\left[\frac{\alpha}{\alpha_p} - \frac{j2\pi^2\beta_2(f_1-f)(f_2-f)}{\alpha_p}\right], -\frac{C_R P_{p_0}}{2\alpha_p} e^{2\alpha_p L_s}\right)\right] \right|^2 \end{aligned} \tag{12}$$

where $\Gamma(x_1, x_2)$ is the upper incomplete Gamma function, defined as $\Gamma(a, x) = \int_x^\infty w^{a-1} e^{-w}\, dw$.

The above result regarding the FWM efficiency in the presence of backward-pumped Raman amplification is original and is described here for the first time. The derivation is lengthy and will not be reported. However, the correctness of the formula can be easily checked vs. numerical integration of the defining integral shown above. For convenience, the formula for ASE noise from Raman amplification is provided in Appendix J, which is needed to estimate $\mathrm{OSNR}_{\mathrm{tot}}$.

XI. Approximate Solutions to the GNRF

The GNRF cannot be solved analytically. However, useful approximations can be derived, which can be of help in carrying out preliminary performance assessments, or be the basis for real-time, physical-layer awareness computation for flexible wavelength-routed networks.

A. Nyquist-WDM over a single span

In the Nyquist-WDM case, over a single span, an approximate but accurate solution of the GNRF can be found, as shown in Appendix F. The final result is:

$$G_{\mathrm{NLI}}\left(0\right) \approx \frac{8}{27}\gamma^2 G_{\mathrm{WDM}}^3 L_{\mathrm{eff}}^2 \frac{\operatorname{asinh}\left(\frac{\pi^2}{2}\beta_2 L_{\mathrm{eff,a}} B_{\mathrm{WDM}}^2\right)}{\pi\beta_2 L_{\mathrm{eff,a}}} \tag{13}$$

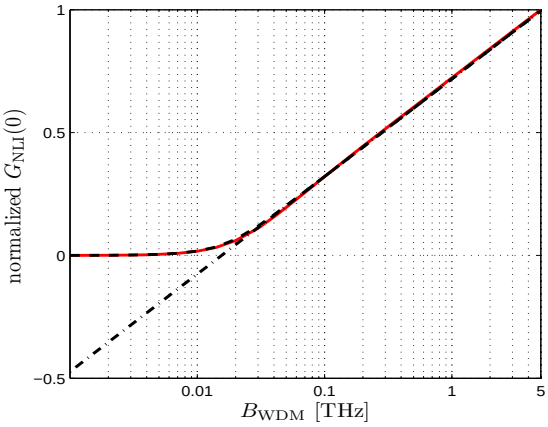

Fig. 14. Plot of $G_{\mathrm{NLI}}(0)$ vs. B_{WDM} for the NY-SMF case after a single span. Red solid line: accurate numerical integration of the GNRF; dashed line: Eq. (13); dashed-dotted line: Eq. (14). All curves normalized to the max of the solid line, for ease of comparison.

where 'asinh' is the hyperbolic arcsin function. For large x, $\operatorname{asinh}(x) \approx \log_e(2x)$, with a relative error of less than 1% when $x > 3.5$. If so, then:

$$G_{\mathrm{NLI}}\left(0\right) \approx \frac{8}{27}\gamma^2 G_{\mathrm{WDM}}^3 L_{\mathrm{eff}}^2 \frac{\log_e\left(\pi^2\beta_2 L_{\mathrm{eff,a}} B_{\mathrm{WDM}}^2\right)}{\pi\beta_2 L_{\mathrm{eff,a}}} \tag{14}$$

Note that there is a slight difference between this formula and the one shown in [12], due to the further approximation made there of $L_{\mathrm{eff}} \approx L_{\mathrm{eff,a}}$. Formulas similar to Eq. (14) can be found in some of the papers dealing with perturbative models discussed in Sect. II, such as [4]–[6] and [10].

As an example of the accuracy that can be expected out of Eqs. (13)-(14), Fig. 14 shows $G_{\mathrm{NLI}}(0)$ vs. B_{WDM}, for the NY-SMF case: the solid line is the result of accurate numerical integration of the GNRF; the dashed line is Eq. (13) and the dashed-dotted line is Eq. (14). The agreement of both approximations is excellent down to about B_{WDM}=25 GHz. Below this value, Eq. (13) keeps being very accurate whereas Eq. (14) departs sharply from the exact curve. At low 'log' arguments it even returns non-physical (negative) results.

Note that if the span loss is smaller than about 7 dB, the approximation Eq. (36) starts breaking down, causing loss of accuracy of both Eqs. (13)-(14).

B. Non-Nyquist-WDM over a single span

The non-Nyquist case for N_s=1 requires the integration of the GNRF over a complex-shaped domain such as shown in Fig. 3. Various approximate solutions are shown in Appendix G. The simplest and most intuitive formula is the following:

$$G_{\mathrm{NLI}}(0) \approx \tfrac{8}{27}\frac{\gamma^2 G_{\mathrm{WDM}}^3 L_{\mathrm{eff}}^2}{\pi\beta_2 L_{\mathrm{eff,a}}} \operatorname{asinh}\left(\tfrac{\pi^2}{2}\beta_2 L_{\mathrm{eff,a}} B_{\mathrm{ch}}^2 N_{\mathrm{ch}}^{2\frac{B_{\mathrm{ch}}}{\Delta f}}\right) \tag{15}$$

Note that if $B_{\mathrm{ch}} = \Delta f$ is imposed, then:

$$B_{\mathrm{ch}}^2 N_{\mathrm{ch}}^{2\frac{B_{\mathrm{ch}}}{\Delta f}} = B_{\mathrm{WDM}}^2$$

and the Nyquist WDM formula Eq. (13) is correctly found.

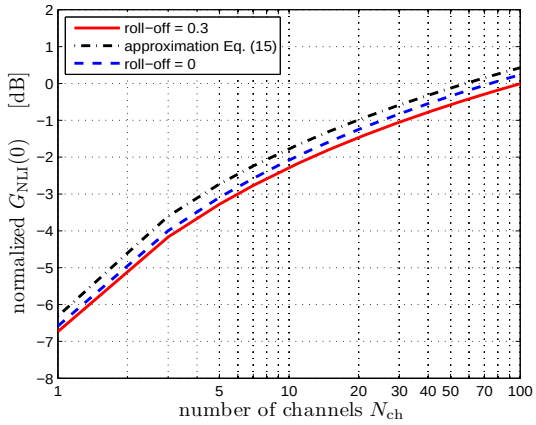

Fig. 15. Plot of $G_{\rm NLI}(0)$ in dB, vs. number of channels $N_{\rm ch}$ for the NY-SMF case after a single span. Red solid line: accurate numerical integration of the GNRF with roll-off=0.3; blue dashed line: same, but with roll-off=0; black dash-dotted line: Eq. (15). All curves normalized to the max of the solid line, for ease of comparison.

In Fig. 15 a comparison is shown between exact values of $G_{\rm NLI}(0)$ and Eq. (15), as a function of the number of channels $N_{\rm ch}$. The solid curve is found through accurate numerical integration of the GNRF for RS-SMF. The middle dashed curve is the same as the previous one, but with roll-off=0, that is is with rectangular channel spectra whose bandwidth is exactly $B_{\rm ch}$=R_s. Finally, the top curve (dash-dotted) is Eq. (15). The agreement between Eq. (15) and the case with roll-off=0 is quite good. At 101 channels (C-band) the difference is about 0.2 dB.

The agreement is somewhat less good with the case roll-off=0.3, because Eq. (15) intrinsically assumes rectangular spectra, as an approximation. Even so, the error is relatively small, less than 0.5 dB at full C-band, making Eq. (15) an effective tool for fast approximate calculations. In passing, notice the interesting circumstance that channels with same R_s but larger roll-off produce slightly less NLI (bottom vs. middle curve). Not shown for brevity, the results for RS-LPSCF and RS-NZDSF indicate similar accuracy as for the RS-SMF case.

Note that due to the nature of the approximations involved, Eq. (15) may not be reliable when used outside of the following parameter boundaries: span loss $\geq$7 dB, $\beta_2 \geq 4$, $R_s \geq 28$ GBaud and $B_{\rm ch}/\Delta f \geq 0.25$.

Alternatively, Eq. (40) derived in Appendix G can be used. This formula is rather reliable in estimating the GNRF across all parameter values, to better than $\pm$1 dB, with the only limitation of span loss $\geq$7 dB. On the other hand, it is more complex and less intuitive. An even more accurate formula is Eq. (39), which however contains special functions.

Finally, in Eq. (15) 'asinh' could be replaced with 'log' of twice the argument of the asinh, provided that such argument is greater than 3.5, as discussed in the previous section.

C. Nyquist-WDM with multiple spans

When N_s >1 the phased-array factor χ of the GNRF comes into play. Quite interestingly, besides the compact form of Eq. (3), χ can also be written in sum form:

$$\chi(f_1,f_2,f) = N_s + \\ +2\sum_{n=1}^{N_s-1}(N_s-n)\cdot\cos\left(4n\,\pi^2\beta_2 L_s\,(f_1-f)\,(f_2-f)\right) \tag{16}$$

When this alternative expression is inserted into the GNRF, the latter splits into two contributions:

$$G_{\rm NLI}(f) = G^{\rm inc}_{\rm NLI}(f) + G^{\rm cc}_{\rm NLI}(f) \tag{17}$$

where the first one represents purely *incoherent* noise accumulation:

$$G^{\rm inc}_{\rm NLI}(f) = N_s\cdot G_{\rm NLI}(f)\,|_{N_s=1} \tag{18}$$

and the second one represents a sort of *coherence correction*:

$$G^{\rm cc}_{\rm NLI}(f) = \tfrac{32}{27}\gamma^2 L_{\rm eff}^2 \sum_{n=1}^{N_s-1}(N_s-n)\cdot \\ \int_{-\infty}^{\infty}\int_{-\infty}^{\infty} G_{\rm WDM}(f_1)G_{\rm WDM}(f_2)G_{\rm WDM}(f_1+f_2-f)\cdot \\ \rho(f_1,f_2,f)\cdot\cos\left(n\cdot 4\pi^2|\beta_2|L_s(f_1-f)(f_2-f)\right)\,df_2\,df_1 \tag{19}$$

The integrand function within $G^{\rm cc}_{\rm NLI}$ is not always positive but rather contains an oscillating cosine factor. This suggests that the 'cc' term could be in many cases relatively small versus the 'inc' term. This conjecture is confirmed by the numerical results of Sect. IX, at least for large $B_{\rm WDM}$. If so, an obvious lowest-order analytical approximation is:

$$G_{\rm NLI}(f) \approx G^{\rm inc}_{\rm NLI}(f)$$

which was used for instance in [12] to obtain Eq. (5) there.

Finding a more accurate result requires finding a closed-form approximation for the double integral in $G^{\rm cc}_{\rm NLI}$. This is possible for the Nyquist-WDM case, at the center frequency $f=0$. The main mathematical steps are outlined in Appendix H. The final result is:

$$G^{\rm cc}_{\rm NLI}(0) \approx \frac{16}{27}\frac{\gamma^2 L_{\rm eff}^2}{\pi\beta_2 L_s}\left[1-N_s+N_s\,{\rm HarNum}\,(N_s-1)\right] \tag{20}$$

where ${\rm HarNum}\,(k)$ is the k-th harmonic number.

It is then possible to relate this formula to the heuristic but quite accurate model of NLI noise accumulation of Eq. (7). By equating Eq. (7) to Eq. (17), and concentrating on $f=0$, one can write:

$$\epsilon = \log_e\left(1+\frac{G^{\rm cc}_{\rm NLI}(0)}{G^{\rm inc}_{\rm NLI}(0)}\right)\cdot\frac{1}{\log_e(N_s)} \tag{21}$$

Then using Eqs. (13), (17) and (20), an approximate formula for ϵ can be written as:

$$\epsilon \approx \frac{\log_e\left(1+\frac{2L_{\rm eff,a}}{N_s L_s}\frac{[1-N_s+N_s{\rm HarNum}(N_s-1)]}{{\rm asinh}\left(\frac{\pi^2}{2}\beta_2 L_{\rm eff,a}B^2_{\rm WDM}\right)}\right)}{\log_e(N_s)} \tag{22}$$

The above formula shows that ϵ is a function of N_s. This appears to contradict the numerical results found in Sect. IX, which hinted at a single ϵ being capable of modeling NLI accumulation across all values of N_s, for a given system. Fig. 16 solves this apparent paradox. ϵ is plotted vs. N_s using both accurate numerical integration of the GNRF and Eq. (22),

for the NY-SMF system (C-band). The figure shows that ϵ varies very little vs. N_s, to the point that it can indeed be considered a constant. Additionally, the approximate formula Eq. (22) appears to provide a rather accurate estimate of ϵ. A slight loss of accuracy occurs only for low values of N_s, due to some of the approximations used to find Eq. (20) being less reliable at low N_s.

Since the exact numerical results indicate that ϵ is virtually constant, it appears that a simpler approximation could be obtained by extracting such constant value from Eq. (22). This can be done through a series expansion of Eq. (22) at high N_s, where it better coincides with the exact value, then truncated to zero-th order. The following formula is thus found:

$$\epsilon \approx \frac{3}{10} \cdot \log_e \left(1 + \frac{6}{L_s} \frac{L_{\mathrm{eff,a}}}{\operatorname{asinh}\left(\frac{\pi^2}{2} \beta_2 L_{\mathrm{eff,a}} B_{\mathrm{WDM}}^2 \right)} \right) \qquad (23)$$

Fig. 16 shows it to be quite accurate. Not shown for brevity, it provides the same high degree of accuracy for NY-NZDSF and NY-LPSCF as well.

In Fig. 17, the accuracy of Eq. (23) is probed vs. B_{WDM}, for a NY-NZDSF system. The formula is very accurate down to 40 GHz. For lower B_{WDM}, some of the approximations used in calculating $G_{\mathrm{NLI}}^{\mathrm{cc}}$ break down and accuracy is lost. With NY-SMF and NY-LPSCF the high accuracy range actually extends further down to about 20 GHz (not shown). This accuracy limit can be made more general, as follows: Eq. (23) is accurate as long as the argument of the asinh is larger than 1. Below this value the formula cannot be used.

Finally, Fig. 18 compares numerical results with Eq. (23), vs. span length L_s, for the NY-SMF system (C-band). Here too, accuracy is very good, with some slight disagreement at low span length.

In summary, Eq. (23) appears to be a good approximate tool, sufficiently reliable to perform preliminary performance assessment and capable of clearly indicating the trends of ϵ vs. the main system parameters. Incidentally, it can be observed that, for fully populated systems (C-band), the strongest dependence of ϵ is on span length, with ϵ significantly decreasing vs. L_s. This circumstance hints, for instance, at submarine systems experiencing more 'coherent' NLI accumulation than terrestrial.

D. Non-Nyquist-WDM with multiple spans

For the non-Nyquist case, a closed-form estimate of $G_{\mathrm{NLI}}^{\mathrm{cc}}$ is not yet available. However, a coarse approximate formula can be written, based on the assumption that $G_{\mathrm{NLI}}^{\mathrm{cc}}$ is the same as that of the Nyquist case, while $G_{\mathrm{NLI}}^{\mathrm{inc}}$ is given by Eq. (15):

$$\varepsilon \approx \frac{3}{10} \cdot \log_e \left(1 + \frac{6}{L_s} \frac{L_{\mathrm{eff,a}}}{\operatorname{asinh}\left(\frac{\pi^2}{2} \beta_2 L_{\mathrm{eff,a}} B_{\mathrm{ch}}^2 [N_{ch}^2] \frac{B_{ch}}{\Delta f} \right)} \right)$$

This formula turns out to typically underestimate ϵ by 5% to 20%. Its accuracy is therefore limited, but the main parameter dependencies appear to be correctly captured by it. Note that it cannot be used outside of the parameter range of validity of Eq. (15), indicated at the end of Sect. XI-B.

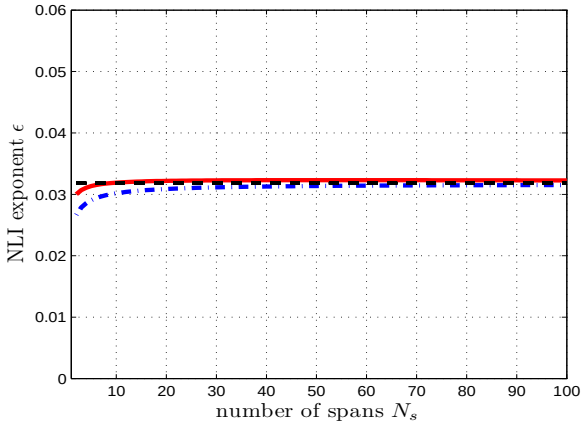

Fig. 16. Plot of the NLI exponent ϵ appearing in Eq. (7), vs. number of spans N_s for the NY-SMF system using the full C-band. Red solid line: accurate numerical integration of the GNRF. Blue dash-dotted line: Eq. (22). Black thin dashed line: Eq. (23).

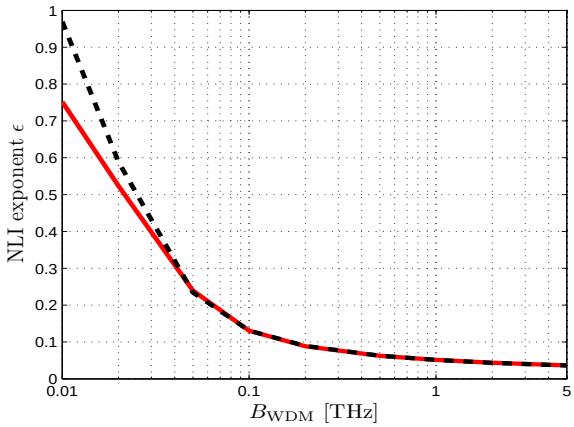

Fig. 17. Plot of the NLI exponent ϵ appearing in Eq. (7), vs. system optical bandwidth B_{WDM} for the NY-SMF system. Red solid line: accurate numerical integration of the GNRF. Black dashed dashed line: Eq. (23).

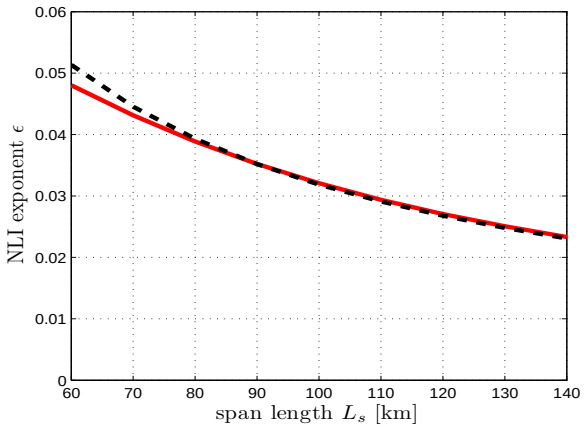

Fig. 18. Plot of the NLI exponent ϵ appearing in Eq. (7), vs. span length L_s for the NY-SMF system. Red solid line: accurate numerical integration of the GNRF. Black dashed line: Eq. (23).

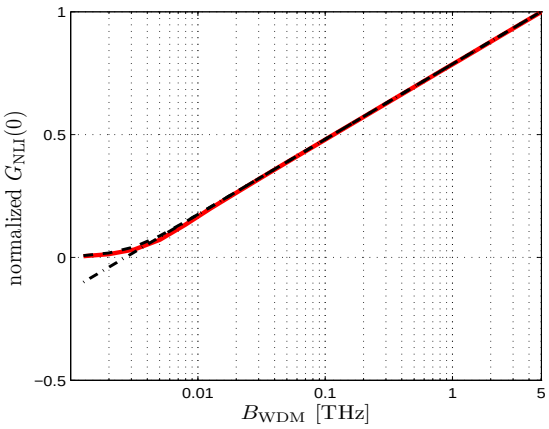

Fig. 19. Plot of $G_{\rm NLI}(0)$ vs. $B_{\rm WDM}$ for the NY-SMF case assuming a single span of length 1,000 km and ideal distributed amplification. Red solid line: accurate numerical integration of the GNRF; dashed line: Eq. (24); dashed-dotted line: Eq. (24) with $\mathrm{asinh}(x)$ replaced by $\log_e(2x)$. All curves normalized to the max of the solid line, for ease of comparison.

E. Ideal Distributed Amplification

Another instance in which an analytical approximate solution of the GNRF can be found is when the signal is Nyquist-WDM and amplification is ideally distributed, that is $g(z) = \alpha$. Note that in this case the concept of 'span' loses meaning: the fiber is homogeneous from the beginning to the end of the link.

A very accurate formula, whose detailed derivation is reported in App. I, is given by:

$$G_{\rm NLI}(0) \approx \frac{16}{27}\gamma^2 G_{\rm WDM}^3 L_{\rm tot} \frac{\mathrm{asinh}\left(\frac{1}{3}\pi^2\beta_2 L_{\rm tot} B_{\rm WDM}^2\right)}{\pi\beta_2} \quad (24)$$

Here too $\mathrm{asinh}(x)$ can be replaced by $\log_e(2x)$ when $x > 3.5$. In Fig. 19 a comparison between Eq. (24) and the results of the accurate numerical integration of the GNRF is shown, vs. $B_{\rm WDM}$, for the NY-SMF case assuming a single span of length 1,000 km and ideal distributed amplification. The log approximation is also plotted. Eq. (24) appears to deliver very accurate $G_{\rm NLI}$ values throughout.

This formula is a powerful result, which can for instance be used to find the ultimate performance of optical systems over an ideal distributed-amplification link. Fundamental capacity limits can be derived from it as well, as it was done in [23].

Note that Eq. (24) appears very similar to the conventional lossy fiber formula Eq. (13), provided that $L_{\rm eff,a}$ and $L_{\rm eff}$ are replaced by $L_{\rm tot}$. However, both the leading fraction and the asinh argument constants are different. In fact, Eq. (24) cannot be directly derived from Eq. (13). More details about this aspect can be found in Appendix I.

XII. System Implications of the GN Model

The GN model allows to predict system performance, based on $\mathrm{OSNR}_{\rm tot}$ introduced as Eq. (4). How to use such OSNR to compute the system BER was extensively discussed in [1] and will not be repeated here.

Under the assumption of identical spans, and of span loss exactly compensated for at each span, Eq. (4) can be re-written as:

$$\mathrm{OSNR}_{\rm tot} = \frac{P_{\rm ch}}{P_{\rm ASE}^{(1)} \cdot N_s + p_{\rm NLI}^{(1)} \cdot N_s^{1+\epsilon} \cdot P_{\rm ch}^3 \cdot (B_{\rm ch}^{\rm eq})^{-3}} \quad (25)$$

where $P_{\rm ASE}^{(1)}$ is the ASE noise power after one span and $p_{\rm NLI}^{(1)}$ is the NLI noise accumulated after one span and normalized with respect to the per-channel power $P_{\rm ch}$ and the channel equivalent bandwidth $B_{\rm ch}^{\rm eq}$. For the center channel and according to the 'locally white' NLI noise approximation discussed in Sect. VII:

$$p_{\rm NLI}^{(1)} = G_{\rm NLI}^{(1)}(0) \cdot B_N \cdot P_{\rm ch}^{-3} \cdot (B_{\rm ch}^{\rm eq})^3 \quad (26)$$

where $G_{\rm NLI}^{(1)}(0)$ is the NLI PSD after one span at f=0, B_N is the chosen OSNR noise bandwidth and $B_{\rm ch}^{\rm eq}$ is defined as:

$$B_{\rm ch}^{\rm eq} = \frac{P_{\rm ch}}{G_{\rm WDM}(0)} \quad (27)$$

Also, note that in Eq. (25) the 'coherent' NLI span accumulation law $N_s^{1+\epsilon}$ of Eq. (7) is assumed.

In essence, once $P_{\rm ASE}^{(1)}$ and $p_{\rm NLI}^{(1)}$ have been assessed based on signal spectrum and system span parameters, all the scaling vs. number of spans and launch power is provided by Eq. (25), which hence represents a simple and powerful analysis/design tool.

The first key quantity that can be derived from it is the *optimum launch power per channel* $P_{\rm ch,opt}$. Power can be optimized for minimum BER, maximum number of spans, or for maximum span loss at a fixed number of spans. In this paper, the first two cases are dealt with. The third one will be omitted for brevity.

A. Minimizing the BER

Minimizing the BER at a fixed distance is accomplished by maximizing the OSNR. The launch power per channel which maximizes Eq. (25) is readily found as :

$$P_{\rm ch,opt}^{(\rm BER)} = B_{\rm ch}^{\rm eq} \sqrt[3]{\frac{P_{\rm ASE}^{(1)}}{2p_{\rm NLI}^{(1)} N_s^{\epsilon}}} \quad (28)$$

If $P_{\rm ch,opt}^{(\rm BER)}$ is inserted back into Eq. (25), it is immediately seen that the overall ASE noise term at the denominator is always twice the overall NLI noise term, for any ϵ. In other words, the minimum BER (or maximum OSNR) is always obtained when $P_{\rm ASE} = 2P_{\rm NLI}$ in Eq. (4). This result, was first pointed out in [24] and then experimentally confirmed in [15]. It is significant because it shows that top performance is achieved, for any transmission format, in a situation where NLI noise is relatively 'small' vs. ASE noise. Put it differently, optimal operation does not entail a 'high non-linearity' regime, where NLI noise is prevailing.

Note that the GN model is a perturbative model and therefore it can be expected to be accurate only at a relatively low level of non-linearity. On the other hand, it appears that relatively low non-linearity is where optimum operation occurs and hence this circumstance supports the reliability of the model.

B. Maximizing the number of spans

Unfortunately, no closed-form expression of the power maximizing the number of spans $P_{\mathrm{ch,opt}}^{(N_s)}$ exists for a generic ϵ, although it can easily be calculated numerically from Eq. (25). However, as pointed out in Sect. IX-A, in C-band systems $\epsilon \approx 0$. With this approximation, then it turns out that $P_{\mathrm{ch,opt}}^{(N_s)}$ coincides with $P_{\mathrm{ch,opt}}^{(\mathrm{BER})}$:

$$P_{\mathrm{ch,opt}}^{(N_s)} = B_{\mathrm{ch}}^{\mathrm{eq}} \sqrt[3]{\frac{P_{\mathrm{ASE}}^{(1)}}{2p_{\mathrm{NLI}}^{(1)}}} \tag{29}$$

and, as a result, here too the optimum occurs when $P_{\mathrm{ASE}} = 2P_{\mathrm{NLI}}$. The corresponding maximum $N_s^{\max}$ is:

$$N_s^{\max} = \frac{B_{\mathrm{ch}}^{\mathrm{eq}}}{3\,\mathrm{OSNR_T}} \sqrt[3]{\frac{4}{\left(P_{\mathrm{ASE}}^{(1)}\right)^2 p_{\mathrm{NLI}}^{(1)}}} \tag{30}$$

where $\mathrm{OSNR_T}$ is the 'target' OSNR, that is the one which is implied by the BER constraints imposed at the end of the link. Note the straight inverse proportionality that holds between $N_s^{\max}$ and $\mathrm{OSNR_T}$, as in the case of pure ASE noise.

An important remark, with far-reaching system impact, is that the optimum launch power is independent of the target OSNR. This in turn leads to the counter-intuitive result that $P_{\mathrm{ch,opt}}^{(N_s)}$ does not depend on either transmission format or transceiver impairments. In other words, there is a very strong de-coupling between link optimization and transceiver optimization, which can be dealt with separately and independently. More comments on this circumstance are proposed later on.

According to Eq. (29), $P_{\mathrm{ch,opt}}^{(N_s)}$ depends on the symbol rate, both because of the explicit factor $B_{\mathrm{ch}}^{\mathrm{eq}}$ and because $p_{\mathrm{NLI}}^{(1)}$ in general depends on it. A different situation is found for the optimum signal peak power spectral density $G_{\mathrm{WDM,opt}}^{(N_s)}(0)$, whose expression is:

$$G_{\mathrm{WDM,opt}}^{(N_s)}(0) = \frac{P_{\mathrm{ch,opt}}^{N_s}}{B_{\mathrm{ch}}^{\mathrm{eq}}} = \sqrt[3]{\frac{P_{\mathrm{ASE}}^{(1)}}{2p_{\mathrm{NLI}}^{(1)}}} \tag{31}$$

The factor $B_{\mathrm{ch}}^{\mathrm{eq}}$ is no longer present in the rightmost-hand side. Also, assuming Nyquist-WDM and a constant total system B_{WDM}, $p_{\mathrm{NLI}}^{(1)}$ does not depend on the symbol rate R_s either, as shown by Eq. (13), and therefore $G_{\mathrm{WDM,opt}}^{(N_s)}(0)$ becomes completely independent of R_s. Therefore, at least in the Nyquist-WDM case, the optimum signal PSD is independent of format, transceiver impairments *and symbol rate*. It only depends on the span structure and on the total system optical bandwidth B_{WDM}.

To provide a few numerical examples, in the case of RS-SMF (full C-band, EDFA noise figure 6 dB), using Eq. (29), the optimum launch power spectral density $G_{\mathrm{WDM,opt}}^{(N_s)}(0)$ turns out to be 28.5 [μW/GHz], or -0.4 dBm per channel, amounting to about 20 dBm overall. Assuming NY-SMF (full C-band) $P_{\mathrm{ch,opt}}^{(N_s)}(0)$ goes down only slightly, to about -1 dBm per channel. Shortening the span length to 75 km, with NY-SMF, $P_{\mathrm{ch,opt}}^{(N_s)}(0)$ goes further down to -2.6 dBm per channel.

Once again, these results are found assuming $\epsilon \approx 0$ which, for full C-band systems, is often a good approximation. Note that in non-Nyquist-WDM systems with tight channel spacing, $p_{\mathrm{NLI}}^{(1)}$ is only weakly dependant on the symbol rate and therefore, as an approximation, $G_{\mathrm{WDM,opt}}^{(N_s)}(0)$ can be considered roughly symbol-rate independent in those systems too.

Another important result, that is derived directly from Eq. (30), is the variation in maximum number of spans that occurs when NLI grows or shrinks. The relationship, in dB, is:

$$\Delta N_s^{\max}\ [\mathrm{dB}] = -\frac{1}{3}\Delta p_{\mathrm{NLI}}^{(1)}\ [\mathrm{dB}] \tag{32}$$

where Δ represents the ratio of two values of the relevant quantity.

This formula shows, in one instance, that an approximate assessment of $p_{\mathrm{NLI}}^{(1)}$ which is, say, 0.5 dB in error, causes only a 1/6 dB (that is 4%) error in the estimate of $N_s^{\max}$. This low sensitivity of system performance estimates vs. NLI estimation errors makes the approximate formulas of $G_{\mathrm{NLI}}(0)$ introduced in Sect. XI attractive for practical use.

In another instance, Eq. (31) suggests that any counter-measure that may combat $p_{\mathrm{NLI}}^{(1)}$, such as electronic mitigation, only gains 1/3 dB of maximum reach per 1 dB of $p_{\mathrm{NLI}}^{(1)}$ abatement. This result shows that for non-linearity mitigation strategies to be truly effective, they must grant very large non-linearity cancellation, which may be difficult due to the resulting receiver bandwidth requirements, as discussed in Sect. IX-C.

C. The GN model and link/network optimization

The above results, if confirmed by ongoing research, may have a deep impact on the design of future transmission links and networks. The independence of each span optimum launch power density on format, transmitter impairments, symbol rate (approximately) and previous or subsequent spans features, means that a possible optimization strategy could only look at each span parameters and, specifically, fiber parameters and length, and EDFA noise figure.

The above strategy would imply that *local optimization* of each span would be enough to ensure *global optimization* (the LOGO strategy), a principle that could potentially greatly ease network design and management. Also, once a link or a network has been built, any improvement in transceiver technology, or any change in symbol rate or format, would not require any re-optimization of the launch power densities into any span.

However, a thorough validation of such optimization criteria is necessary. It is also necessary to investigate the effects on the GN-model accuracy of the possibly very different accumulated chromatic dispersion of each channel in any given span of a meshed network.

D. Combating NLI

As mentioned in Sects. IX-C and XII-B, electronic NLI mitigation appears to be useful only to a relatively limited extent, even assuming ideal algorithm effectiveness, at least

under the hypothesis of uncompensated transmission made throughout this paper.

Regarding optical NLI mitigation, Eqs. (13) and (15) indicate two possible ways to perform it: increasing dispersion and decreasing the non-linearity coefficient γ. In fact, using Eq. (13) or Eq. (15) to express $p_{\mathrm{NLI}}^{(1)}$ in Eq. (32) and neglecting weak logarithmic dependencies, the following two relations can be found:

$$\Delta N_s^{\max}[\mathrm{dB}] = \frac{1}{3}\Delta\beta[\mathrm{dB}]$$

$$\Delta N_s^{\max}[\mathrm{dB}] = -\frac{2}{3}\Delta\gamma[\mathrm{dB}] = \frac{2}{3}\Delta A_{\mathrm{eff}}[\mathrm{dB}]$$

The top formula shows that any increase of x dB in β_2 (or D) would result in $\frac{x}{3}$ dB reach increase. However, the current value of β_2 ≈27 ps^2/nm, corresponding to D ≈21.5 ps/(nm·km), typical of modern PSCFs, appears difficult to increase further. Very large negative D values are possible, and have been achieved in dispersion compensating fibers, but they are generally obtained at the cost of a drastic increase in loss and γ, which completely offsets any potential advantage.

On the other hand, a reduction of x dB of γ or increase of x dB of A_{eff} brings about a $\frac{2x}{3}$ dB reach increase. The doubled coefficient is due to γ appearing squared in both Eq. (13) and Eq. (15). From a technological viewpoint, this strategy appears attractive: experimental fibers with effective areas up to 150 μm^2 have already been used in record experiments and it seems that even larger values may be feasible. Here too, however, there are limitations. In particular, bend loss may considerably go up as A_{eff} is further increased, possibly offsetting the potential advantage.

In summary, at present, within the context of UT, the most potentially effective countermeasure to NLI, according to the the results of the GN model, appears to be the manufacturing of fibers with large mode effective areas, provided that this does not result in substantial loss increase.

XIII. Conclusion

In this paper, the GN model was extensively discussed. Similar models and validation efforts were reviewed. Where possible, intuitive physical interpretations of the model features were proposed. Techniques for a more effective exploitation of the model were presented, together with some extensions aimed at making it more encompassing for system studies and analysis. New approximate closed-form analytical solutions were proposed. Some of the implications of the model could have a substantial impact on system and network design and optimization, as well as on non-linearity mitigation, and these aspects were discussed.

Ample room is still available for further research on the GN model. For instance: closed-form analytical results which are more accurate and/or encompass a wider range of system scenarios; a broader exploration of the validity envelope of the model, especially towards very low dispersion values and low symbol rates, where signal 'gaussianization' after launch is slow, and for mixed fiber systems; model extensions aiming at encompassing dispersion-managed systems. Experimental validation tests are also greatly needed, as in the end what matters is obviously not the agreement of the model with simulations but rather with actual, physical systems.

All in all, however, the GN model already appears to capture at least the main features of non-linear propagation in UT coherent systems. As a result, it is a promising candidate for being a useful tool for system and network analysis design and control.

XIV. Acknowledgements

The author would like to thank G. Bosco, A. Carena, R. Cigliutti and V. Curri from Politecnico di Torino, A. Nespola from Istituto Superiore Mario Boella, F. Forghieri, R. Pastorelli and S. Piciaccia from CISCO Photonics, M. Schiano, E. Riccardi and A. Pagano from Telecom Italia, for their insightful comments and the useful and motivating discussions.

Appendix

Appendix A
Integration Islands for Small Channel Spacings

When the channel spacing is smaller than 3/2 of the channel bandwidth, that is $B_{\mathrm{ch}} > \frac{2}{3}\Delta f$, the simple islands appearing in Fig. 3 are compounded by a number of smaller triangular islands, an example of which is shown in Fig. 20. As the channel spacing shrinks, these small triangles actually fill the gaps among the lozenge-shaped islands, so that when B_{ch}=Δf then the integration domain becomes compact as shown in Fig. 1.

From the viewpoint of the taxonomy of NLI, the lozenge-shaped islands classification shown in Fig. 3 is still valid if mapped onto Fig. 20. Regarding the triangular-shaped regions, they too can be classified as SCI, XCI or MCI, although in a less intuitive way. For instance, the triangle to the right and above the center island is XCI and not SCI as it could otherwise be guessed by its proximity to the center island.

On the other hand, it is clear that as the Nyquist-WDM situation is approached, any taxonomy based on 'islands' tends to lose meaning since the integration domain joins up seamlessly, within the boundaries of Fig. 1.

Appendix B
Brute-Force GNRF Integration

A brute-force approach to GNRF numerical integration may consist of integrating the GNRF over the square domain $f_1, f_2 \in [-B_{\mathrm{WDM}}/2, B_{\mathrm{WDM}}/2]$. One favorable aspect of the integrand of the GNRF is that it is everywhere positive and therefore one could simply keep on tightening the accuracy parameter of the integration algorithm till an apparent saturation of the result is reached. However, it typically turns out that convergence is very slow, especially when a large B_{WDM} is involved. Unfortunately, it is the large B_{WDM} case that is of the greatest interest for system design purposes, up to the whole C band (5 THz) or even the C+L band case (11 THz).

The difficulty in performing the numerical integration of the GNRF mostly stems from the phased-array factor of the

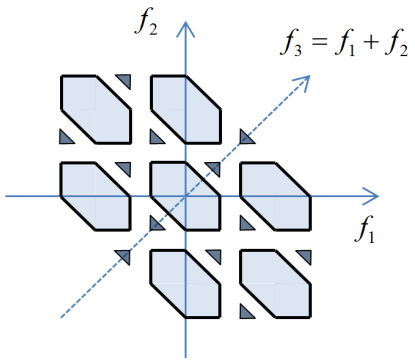

Fig. 20. Integration domain 'islands' of the GNRF, when the transmitted signal is made up of 3 equally-spaced identical channels with $\frac{2}{3}\Delta f < B_{\rm ch} < \Delta f$. Notice the small triangular islands (darker shading) that are not present when $B_{\rm ch} \leq \frac{2}{3}\Delta f$.

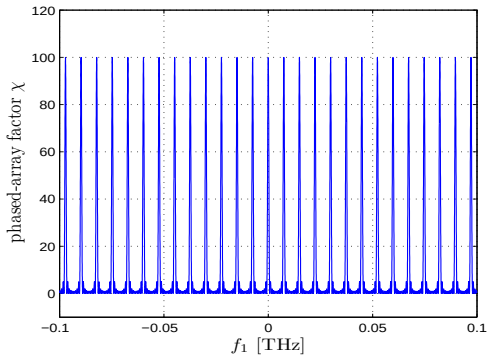

Fig. 21. Plot of the phased-array factor $\chi(f_1, f_2, 0)$, present in the integrand of the GNRF, with N_s =10 spans, shown for f_2=10 GHz and $f_1 \in [-0.1, 0.1]$ THz.

integrand function, $\chi(f_1, f_2, f)$, defined in Eq. (3). Such factor presents very sharp peaks, whose height is exactly N_s^2 and whose width is inversely proportional to N_s. As an example, in Fig. 21 a plot is shown of $\chi(f_1, f_2, f)$ with f_2=10 GHz and f=0, drawn over the relatively limited range $f_1 \in [-0.1, 0.1]$ THz. SMF fiber with N_s=10 is assumed. Clearly, very fine steps would be required for good integration accuracy. Note that if f_2 is doubled, i.e., is set to 20 GHz, the number of peaks also doubles, while their width is halved. At the boundary of the integration domain (f_2=2.5 THz), a total of more than 1.6 million sharp peaks would be found across the f_1 integration range $[-2.5, 2.5]$ THz. Such features of χ make brute-force integration completely impractical.

Brute-force does work in one case, however, namely when N_s=1. If so, the phased-array term disappears and the remainder of the integrand function is well-behaved. On the other hand, the typical scenarios of interest are the multi-span ones. Therefore, it is necessary to study and take advantage of the specific features of the GNRF integrand in order to make its numerical integration possible for multi-span too. In the following appendices, the integrand symmetries and its decay vs. frequency are studied. Eventually, these elements, together with a change of integration coordinates to hyperbolic, can provide a viable technique for the numerical integration of the GNRF.

Appendix C
GNRF integrand symmetries

The GNRF integrand does not change if f_1 and f_2 are swapped, independently of the value of f. This means that its integrand is symmetric with respect to the I-III quadrant bisector. As a result, one could perform the numerical integration of the GNRF only on half of the full integration domain, examples of which are shown in Figs. 1–3. Namely, one could integrate either above or below the f_3 axis and then multiply the result by two.

A stronger symmetry is found if the GNRF is evaluated at f=0 and $G_{\rm WDM}(f)$ is an even function of f. This case is of significant practical interest because, as mentioned in Sect. VII, it is typically enough to evaluate $G_{\rm NLI}(0)$ in order to obtain a fairly accurate assessment of system performance. In addition, the even condition on $G_{\rm WDM}$ is satisfied by many systems, including all systems made up of identical, equally spaced channels. Under these assumptions, f_1 can be swapped with $-f_1$ and f_2 with $-f_2$, simultaneously. This means that the integrand is symmetric with respect to the II-IV quadrant bisector as well. This in turn means that numerical integration can be carried out on only one fourth of the overall integration domain, with the result multiplied by four. Fig. 22 shows one possible sector of the (f_1, f_2) plane providing all the needed information to calculate $G_{\rm NLI}(0)$. Note that formally the sector is unlimited towards the right, but the presence of the WDM spectrum factors in the integrand curtails it to a finite domain, as shown in Fig. 1.

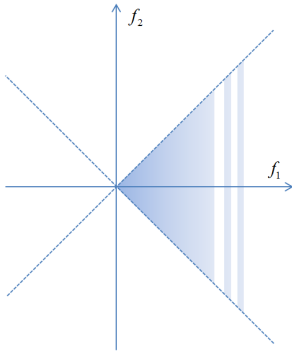

Fig. 22. Shaded: section of the (f_1, f_2) plane providing all the needed information to calculate $G_{\rm NLI}(0)$. Note that formally it is unlimited towards the right. In practice, the presence of the WDM spectrum factors $G_{\rm WDM}(f_1)G_{\rm WDM}(f_2)G_{\rm WDM}(f_1+f_2)$ in the integrand curtails it to a finite domain.

Appendix D
GNRF integrand decay vs. frequency

First, the case of N_s=1 is discussed. Also, for convenience, f=0 is assumed. Under these assumptions, the GNRF becomes:

$$G_{\rm NLI}(0) = \tfrac{16}{27}\gamma^2 L_{\rm eff}^2 \int_{-\infty}^{\infty}\int_{-\infty}^{\infty} \rho(f_1, f_2, 0)\cdot G_{\rm WDM}(f_1)G_{\rm WDM}(f_2)G_{\rm WDM}(f_1+f_2)\, df_2\, df_1 \tag{33}$$

The signal spectrum factors essentially govern the integration domain, whereas the FWM efficiency factor $\rho(f_1, f_2, 0)$, defined by Eq. (2), weighs the contribution of the various frequencies. ρ decreases as $|f_1|$ and $|f_2|$ go up. This decay is depicted in the contour plot of Fig. 7, drawn using SMF parameters. Despite the fact that the plot domain is limited to $f_1, f_2 \in [-0.1, 0.1]$ THz, a decrease down to -40 dB is already visible at the corners of the plot.

Such fast decay of ρ may lead to thinking that the integration domain of the GNRF can be drastically reduced to perhaps a few hundred GHz, all higher frequencies possibly contributing negligibly. Physically speaking, this would mean that NLI is produced only by channels within a few hundred GHz of f=0, all farther channels contributing nothing.

This hypothesis is however incorrect. In Sects. IX and XI it is shown that far-away frequencies still contribute to NLI accumulation. Growth is of the type: $G_{\text{NLI}} \propto \log_e(\text{const} \cdot B_{\text{WDM}})$, hence slow, but without any saturation. More specifically, it appears that XCI contributions continue to play a role even when they originate from very distant channels. As a result, it appears that the integration domain of the GNRF cannot be reduced by simply shrinking the size of the square region of the (f_1, f_2) plane on which the integrand is evaluated.

If $N_s \neq 0$, it can be shown that the presence of the phased-array factor χ does not alter this general picture. Also, $f \neq 0$ does not alter this general picture either.

Therefore, the correct way of exploiting the fast decay of ρ is by switching to hyperbolic coordinates in the GNRF and then curtailing the integration range of ν_1, as shown in Sect. VIII-A. Differently from reducing the square integration domain over (f_1, f_2), which turns out to be inadequate, acting on ν_1 is extremely effective. The reason is that limiting the range over ν_1 does not neglect the XCI contributions from far channels which are incorrectly neglected when shrinking a square (f_1, f_2) domain. In fact, all XCI contributions are duly taken into account, as it can be seen by comparing Fig. 3 with Fig. 8.

A. Curtailing the integration domain

As commented in Sect. VIII-A and above, the integration range over the hyperbolic variable ν_1 in Eq. (5) can typically be reduced substantially because of the presence of the fast-decaying FWM efficiency term ρ. It can be shown that an approximate estimate of the relative error δ incurred by reducing the upper limit of the integration range of ν_1 to $(\mu \cdot B_{\text{WDM}}/2)$, with $\mu \in [0, 1]$, is given by the following formula:

$$\delta \approx 1 - \int_0^{\mu} \frac{4}{1 + \pi^4 (2\alpha)^{-2} \beta_2^2 B_{\text{WDM}}^4 w^4} w \log_e\left(w^{-1}\right) \mathrm{d}w \quad (34)$$

which can be quickly integrated using any mathematical package. It also admits a closed-form analytical solution in terms of special functions (omitted for brevity).

Using for instance RS-SMF parameters, this formula predicts that the error is about 10^{-3} when ν_1 is stopped at only 5% of its total integration range $B_{\text{WDM}}/2$, that is μ=0.05. Another example of error estimation is provided in Fig. 8.

APPENDIX E
DETAILS ON THE DERIVATION OF THE GNRF IN HYPERBOLIC COORDINATES

The case f=0 is addressed first. Also, for now, $G_{\text{WDM}}(f)$ is assumed to be an even function of f and the discussion is limited to the first quadrant of the (f_1, f_2) plane. Formally, the integration domain of the GNRF there is $f_1, f_2 \in [0, \infty]$. However, explicitly taking into account the integration domain limitation due to the $G_{\text{WDM}}(f_1) G_{\text{WDM}}(f_2)$ factor, it is possible to write: $f_1, f_2 \in [0, B_{\text{WDM}}/2]$.

Then, applying to the GNRF the change from cartesian to hyperbolic coordinates in the first-quadrant:

$$\int_0^{B_{\text{WDM}}/2} \int_0^{B_{\text{WDM}}/2} \rho\left(f_1, f_2, 0\right) \cdot \chi\left(f_1, f_2, 0\right) \cdot G_{\text{WDM}}(f_1) G_{\text{WDM}}(f_2) G_{\text{WDM}}(f_1 + f_2) \mathrm{d}f_1 \, \mathrm{d}f_2 =$$

$$= 2 \int_0^{B_{\text{WDM}}/2} \rho\left(\nu_1, 0\right) \cdot \chi\left(\nu_1, 0\right) \cdot |2\nu_1| \cdot \int_0^{\log_e\left(\frac{B_{\text{WDM}}}{2\nu_1}\right)} G_{\text{WDM}}(\nu_1 e^{\nu_2}) G_{\text{WDM}}(\nu_1 e^{-\nu_2}) \cdot G_{\text{WDM}}\left(2\nu_1 \cosh(\nu_2)\right) \mathrm{d}\nu_2 \mathrm{d}\nu_1$$

where $\chi\left(\nu_1, 0\right)$ and $\rho\left(\nu_1, 0\right)$ were defined in Eq. (6).

Note that integration in the right-hand side actually occurs only below the bisector of the first quadrant. However, the contribution above the bisector is identical, because of the symmetries pointed out in Sect. C so it is enough to multiply the result by 2, as is done in the equation.

Addressing then the fourth quadrant, clearly f_2 must be negative. Hyperbolic coordinates are only positive, so it is necessary to explicitly change sign to f_2 in the integrand. Then, applying the change from cartesian to hyperbolic coordinates to the GNRF integral in the fourth-quadrant:

$$\int_{-B_{\text{WDM}}/2}^{0} \int_0^{B_{\text{WDM}}/2} \rho\left(f_1, f_2, 0\right) \cdot \chi\left(f_1, f_2, 0\right) \cdot G_{\text{WDM}}(f_1) G_{\text{WDM}}(f_2) G_{\text{WDM}}(f_1 + f_2) \mathrm{d}f_1 \, \mathrm{d}f_2 =$$

$$= 2 \int_0^{B_{\text{WDM}}/2} \rho\left(\nu_1, 0\right) \cdot \chi\left(\nu_1, 0\right) \cdot |2\nu_1| \cdot \int_0^{\log_e\left(\frac{B_{\text{WDM}}}{2\nu_1}\right)} G_{\text{WDM}}(\nu_1 e^{\nu_2}) G_{\text{WDM}}(\nu_1 e^{-\nu_2}) \cdot G_{\text{WDM}}\left(2\nu_1 \sinh(\nu_2)\right) \mathrm{d}\nu_2 \mathrm{d}\nu_1$$

where the assumption $G_{\text{WDM}}(\nu) = G_{\text{WDM}}(-\nu)$ was exploited. Note that integration in the right-hand side actually occurs only above the bisector of the fourth quadrant. However, the contribution below the bisector is identical, because of the symmetries pointed out in Sect. C, so it is enough to multiply the result by 2, as it was done above.

Finally, by further invoking the symmetries of Sect. C, the two previous results can be multiplied by two to yield the overall result shown in Eq. (5), equivalent to integration on all quadrants. Note however that the actually used integration

domain is located in the first and fourth quadrants, below and above the respective bisectors, in accordance with the symmetry results shown in Appendix C and in particular with Fig. 22.

When the integration domain is further curtailed to speed up approximate numerical integration, as proposed in Sect. VIII-A, then it reduces to the smaller shaded region shown in Fig. 8.

A. Removing all limiting assumptions

In the following, al prior limiting assumptions are removed and a hyperbolic coordinate expression of the GNRF which is valid for $f \neq 0$ and non-even $G_{\mathrm{WDM}}(f)$ is provided.

When $f \neq 0$, both ρ and χ depend only on the product: $(f_1 - f)(f_2 - f)$ and a simple change of integration variables $\theta_1 = (f_1 - f)$, $\theta_2 = (f_2 - f)$ re-creates a dependence on the product $\theta_1\theta_2$ alone. As a consequence of this variable change, the spectral factors G_{WDM} get translated and this must be taken into account to properly determine the integration domain.

Since now $f \neq 0$, the only symmetry that still holds is the one about the I-III quadrant bisector. As a result, one possible set of integration regions on the (θ_1, θ_2) plane which provides all the information about $G_{\mathrm{NLI}}(f)$ is shown in Fig. 23. This set is convenient because both θ_1 and θ_2 do not change sign within each individual region. Therefore, substituting hyperbolic coordinates in these domains is straightforward. Again, since hyperbolic coordinates are positive by definition, when they replace a negative coordinate an explicit minus sign must be added.

The resulting generalized expression of the GNRF is the following:

$$
\begin{aligned}
G_{\mathrm{NLI}}(f) = \tfrac{32}{27}\gamma^2 L_{s,\mathrm{eff}}^2 \int_0^{B_{\mathrm{WDM}}} \rho\,(\nu_1, 0)\,\chi\,(\nu_1, 0)\,|2\nu_1|\cdot \\
\int_0^{\log_e(B_{\mathrm{WDM}}/\nu_1)} [G_{\mathrm{WDM}}(\nu_1 e^{\nu_2} + f)\,G_{\mathrm{WDM}}(\nu_1 e^{-\nu_2} + f)\cdot \\
G_{\mathrm{WDM}}\,(2\nu_1 \cosh(\nu_2) + f) + \\
G_{\mathrm{WDM}}(\nu_1 e^{\nu_2} + f)\,G_{\mathrm{WDM}}(-\nu_1 e^{-\nu_2} + f)\cdot \\
G_{\mathrm{WDM}}\,(2\nu_1 \sinh(\nu_2) + f) + \\
G_{\mathrm{WDM}}(-\nu_1 e^{\nu_2} + f)\,G_{\mathrm{WDM}}(\nu_1 e^{-\nu_2} + f)\cdot \\
G_{\mathrm{WDM}}\,(-2\nu_1 \sinh(\nu_2) + f) + \\
G_{\mathrm{WDM}}(-\nu_1 e^{\nu_2} + f)\,G_{\mathrm{WDM}}(-\nu_1 e^{-\nu_2} + f)\cdot \\
G_{\mathrm{WDM}}\,(-2\nu_1 \cosh(\nu_2) + f)]\,\mathrm{d}\nu_2
\end{aligned}
\tag{35}
$$

Note that the upper limits of the integration range of both ν_1 and ν_2 have been increased with respect to Eq. (5) because the signal spectra now can get translated and therefore the possible integration domain is larger. The new limits can accommodate any value of f producing a non-zero $G_{\mathrm{NLI}}(f)$. The above equation was used to generate $G_{\mathrm{NLI}}(f)$ in Figs. 5 and 6.

On the other hand, as in the case of Eq. (5), the integration range of ν_1 can be curtailed for quick approximate numerical integration. The error can still be estimated using Eq. (34).

B. Further refinements

Both the inner and outer integrals in either Eq. (5) or the more general Eq. (35) can be further improved for ease of integration. The inner integral has the problem of the upper integration limit going to infinity when $\nu_1 \to 0$. The outer integral has the problem of the peaks of χ becoming more frequent and more narrow as ν_1 grows, because the argument of the $\sin^2$ functions within χ contain ν_1^2. Both these problems can be solved by further changing variables within the inner and outer integrals, separately, thus maintaining the general feature of the hyperbolic coordinates, that is the segregation of the χ and ρ factors within the outer integral, and of the spectral terms within the inner integral. The most appropriate specific changes depend on the integration algorithm, so the details are considered outside of the scope of this paper.

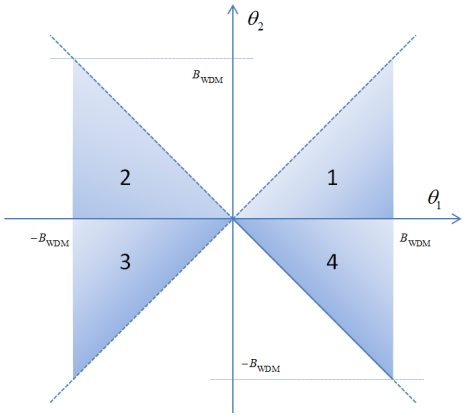

Fig. 23. Actual integration regions used by the GNRF in the form shown in Eq. 35. They can handle any value of f producing non-zero results. The other regions of the plane produce the same result, due to symmetries (see Appendix C).

Appendix F
Derivation of Eq. (13)

Assuming N_s=1 and Nyquist-WDM, the GNRF becomes:

$$
G_{\mathrm{NLI}}\,(0) = \tfrac{16}{27}\gamma^2 G_{\mathrm{WDM}}^2 \int_{-B_{\mathrm{WDM}}/2}^{B_{\mathrm{WDM}}/2} \int_{-B_{\mathrm{WDM}}/2}^{B_{\mathrm{WDM}}/2} \left| \tfrac{1-e^{-2\alpha L_s}e^{j4\pi^2\beta_2 L_s f_1 f_2}}{2\alpha - j4\pi^2\beta_2 f_1 f_2} \right|^2 G_{\mathrm{WDM}}(f_1 + f_2)\,\mathrm{d}f_1\mathrm{d}f_2
$$

where two spectral factors have been replaced by their flat-top values G_{WDM} and their effect on the integration domain is explicitly taken into account in the limits of the integrals.

The third spectral factor $G_{\mathrm{WDM}}(f_1 + f_2)$ is the one causing the clipping-off of the integration domain at the upper corner of the first quadrant and at the lower corner of the third quadrant in the (f_1, f_2) plane, resulting in the lozenge-shaped domain of Fig. 1. Such domain is re-displayed in Fig. 24 marked as $\mathcal{D}$. Using explicitly the symbol $\mathcal{D}$, all three spectral factors become constants and can be taken outside of the integral:

$$
G_{\mathrm{NLI}}\,(0) = \tfrac{16}{27}\gamma^2 G_{\mathrm{WDM}}^3 \iint_{\mathcal{D}} \left| \tfrac{1-e^{-2\alpha L_s}e^{j4\pi^2\beta_2 L_s f_1 f_2}}{2\alpha - j4\pi^2\beta_2 f_1 f_2} \right|^2 \mathrm{d}f_1\mathrm{d}f_2
$$

To obtain an analytical closed-form solution of the above integrals, it is first necessary to approximate the FWM effi-

ciency factor as follows:

$$\left|\frac{1-e^{-2\alpha L_s}e^{j4\pi^2\beta_2 L_s f_1 f_2}}{2\alpha-j4\pi^2\beta_2 f_1 f_2}\right|^2 = \\ = \frac{\left(1-e^{-2\alpha L_s}\right)^2+4e^{-2\alpha L_s}\sin^2\left(2\pi^2\beta_2 f_1 f_2 L_s\right)}{4\alpha^2+16\pi^4\beta_2^2 f_1^2 f_2^2} \approx \\ \frac{\left(1-e^{-2\alpha L_s}\right)^2}{4\alpha^2+16\pi^4\beta_2^2 f_1^2 f_2^2} = \frac{L_{\text{eff}}^2}{1+16\pi^4 L_{\text{eff,a}}^2\beta_2^2 f_1^2 f_2^2} \tag{36}$$

where $L_{\text{eff,a}} = 1/(2\alpha)$ is the asymptotic effective length. The rightmost side is found by neglecting the $\sin^2$ term, which is typically quite small since it is multiplied by the span loss. It should however be kept in mind that if the span loss is very low (less than about 7 dB), accuracy may degrade substantially.

Substituting, one finds:

$$G_{\text{NLI}}(0) \approx \frac{16}{27}\gamma^2 G_{\text{WDM}}^3 \iint_{\mathcal{D}} \frac{L_{\text{eff}}^2}{1+16\pi^4 L_{\text{eff,a}}^2\beta_2^2 f_1^2 f_2^2}\,\mathrm{d}f_1\mathrm{d}f_2 \tag{37}$$

A second approximation is also necessary to achieve a closed-form result: the lozenge-shaped integration domain must be turned into a simpler shape. Two possible alternatives are shown as domains $\mathcal{Q}$ and $\mathcal{C}$ in Fig. 24.

When adopting the square domain $\mathcal{Q}$, the double integral in Eq. (37) can be solved by exploiting the following exact indefinite integrals in sequence:

$$\int \frac{1}{1+\rho^2 x^2}dx = \frac{\tan^{-1}(\rho x)}{\rho}$$

$$\int \frac{\tan^{-1}(\rho x)}{\rho x}dx = \frac{j[\text{Li}_2(-j\rho x)-\text{Li}_2(j\rho x)]}{2\rho}$$

finally yielding:

$$G_{\text{NLI}}(0) \approx \frac{8}{27}\gamma^2 G_{\text{WDM}}^3 L_{\text{eff}}^2 \cdot \\ \frac{j\left[\text{Li}_2\left(-j\pi^2\beta_2 L_{\text{eff,a}} B_{\text{WDM}}^2\right)-\text{Li}_2\left(j\pi^2\beta_2 L_{\text{eff,a}} B_{\text{WDM}}^2\right)\right]}{\pi^2\beta_2 L_{\text{eff,a}}} \tag{38}$$

where Li_2 is a polylogarithm function of order 2 (also called dilogarithm).

When adopting the circular domain $\mathcal{C}$, the double integral in Eq. (37) can be solved by first converting the integration variables (f_1, f_2) into polar variables (φ, r), as follows:

$$\begin{cases} f_1 = r\cos(\varphi) \\ f_2 = r\sin(\varphi) \end{cases}$$

with Jacobian r, then by exploiting the following exact definite integral:

$$\int_0^{2\pi}\int_0^{R} \frac{r}{1+16\pi^4 b^2 r^4 \sin^2(\varphi)\cos^2(\varphi)}\mathrm{d}r\,\mathrm{d}\varphi = \frac{\text{asinh}\left(2bR^2\pi^2\right)}{2b\pi}$$

finally yielding:

$$G_{\text{NLI}}(0) \approx \frac{8}{27}\gamma^2 G_{\text{WDM}}^3 L_{\text{eff}}^2 \frac{\text{asinh}\left(\frac{\pi^2}{2}\beta_2 L_{\text{eff,a}} B_{\text{WDM}}^2\right)}{\pi\beta_2 L_{\text{eff,a}}}$$

Both approximations are quite accurate, with essentially negligible difference between them. A preference could reasonably be awarded to the latter, for the obvious reason that the 'asinh' function is more widely known and commonly available in computer languages and computational tools. Both formulas blend into Eq. (14) under the conditions explained in Sect. XI-A.

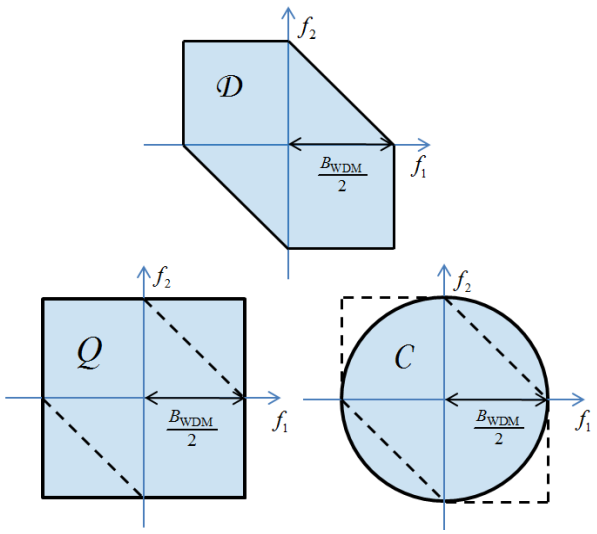

Fig. 24. Plot of the exact domain of integration of the GNRF for the Nyquist case, $\mathcal{D}$, and of two approximations: the square approximation $\mathcal{Q}$ and the circular approximation $\mathcal{C}$. Dashed line: the perimeter of the domain $\mathcal{D}$ to ease comparison with the other domains.

The excellent accuracy of these approximations, despite the substantially modified integration domains, is due to the fact that both of them correctly incorporate the regions of the plane that contribute most to the GNRF, that is those near the f_1 and f_2 axes. See Fig. 7 and App. D for more details.

Appendix G
Derivation of Eq. (15)

The non-Nyquist case requires the integration of the GNRF over a complex-shaped domain such as shown in Fig. 3. In the following various approximate solutions are proposed, for the case N_s=1.

First, each channel is assumed to have a flat spectrum G_{WDM} over its bandwidth B_{ch}, which can however be larger than R_s. Then, the GNRF is integrated over the SCI and XCI lozenges shown in Fig. 3, since they are the ones providing most of the contribution. Each SCI or XCI lozenge is approximated through a small square, similar to the $\mathcal{Q}$ domain in Fig. 24. The individual contribution of each square can be found by extending the calculations of Appendix F. Pulling together all the contributions:

$$G_{\text{NLI}}(0) \approx \frac{16}{27}\gamma^2 L_{\text{eff}}^2 G_{\text{WDM}}^3 \sum_{m=-(N_{\text{ch}}-1)/2}^{(N_{\text{ch}}-1)/2} \cdot (2-\delta_m)\, g_m \tag{39}$$

$$g_m = \\ \frac{j\left[\text{Li}_2\left(-j\pi^2\frac{\beta_2}{\alpha}[m\Delta f+B_{\text{ch}}/2]B_{\text{ch}}\right)-\text{Li}_2\left(j\pi^2\frac{\beta_2}{\alpha}[m\Delta f+B_{\text{ch}}/2]B_{\text{ch}}\right)\right]}{2\pi^2(\alpha)^{-1}\beta_2} - \\ \frac{j\left[\text{Li}_2\left(-j\pi^2\frac{\beta_2}{\alpha}[m\Delta f-B_{\text{ch}}/2]B_{\text{ch}}\right)-\text{Li}_2\left(j\pi^2\frac{\beta_2}{\alpha}[m\Delta f-B_{\text{ch}}/2]B_{\text{ch}}\right)\right]}{2\pi^2(\alpha)^{-1}\beta_2}$$

$$g_0 = \frac{j\left[\text{Li}_2\left(-j\pi^2\beta_2[2\alpha]^{-1}B_{\text{ch}}^2\right)-\text{Li}_2\left(j\pi^2\beta_2[2\alpha]^{-1}B_{\text{ch}}^2\right)\right]}{2\pi^2\beta_2[2\alpha]^{-1}}$$

where δ_m is 1 when $m = 0$ and 0 otherwise.

This formula is very accurate, but contains special functions. The dilogarithm functions can however be approximated using

asinh functions as follows:

$$j\left[\mathrm{Li}_2\left(-jx\right)-\mathrm{Li}_2\left(jx\right)\right]\approx\pi\mathrm{asinh}\left(x/2\right)$$

The final formula is then:

$$\begin{aligned}G_{\mathrm{NLI}}(0)\approx\tfrac{\gamma^2G_{\mathrm{WDM}}^3L_{\mathrm{eff}}^2\left(\frac{2}{3}\right)^3}{\pi\beta_2L_{\mathrm{eff},a}}\cdot\left\{\sum_{\substack{k=-(N_{\mathrm{ch}}-1)/2\\k\neq0}}^{(N_{\mathrm{ch}}-1)/2}\right.\\\left[\mathrm{asinh}\left(\pi^2\beta_2L_{\mathrm{eff},a}B_{\mathrm{ch}}\left[k\Delta f+B_{\mathrm{ch}}/2\right]\right)-\right.\\\mathrm{asinh}\left(\pi^2\beta_2L_{\mathrm{eff},a}B_{\mathrm{ch}}\left[k\Delta f-B_{\mathrm{ch}}/2\right]\right)\Big]+\\\left.\mathrm{asinh}\left(\tfrac{1}{2}\pi^2\beta_2L_{\mathrm{eff},a}B_{\mathrm{ch}}^2\right)\right\}\end{aligned}\tag{40}$$

This formula is quite reliable over the following parameter range: span loss $>$ 7dB (due to the approximation Eq. (36)), $\beta_2\geq3$, $R_s\geq10$ GBaud.

Then, to simplify the result further, it is necessary to resort to the following approximations:

$$\begin{aligned}&\mathrm{asinh}\left(x\right)+\mathrm{asinh}\left(y\right)\approx\mathrm{asinh}\left(2xy\right)&&x,y\gg1\\&\mathrm{asinh}\left(x\right)-\mathrm{asinh}\left(y\right)\approx\mathrm{asinh}\left(\tfrac{x}{2y}\right)&&x,y\gg1,\quad x\gg y\end{aligned}\tag{41}$$

These formulas allow to pull together the sums and differences of the 'asinh' contributions appearing in Eq. (40) into a single asinh, containing the product of the arguments, yielding:

$$\begin{aligned}G_{\mathrm{NLI}}(0)\approx\tfrac{8}{27}G_{\mathrm{WDM}}^3\cdot\tfrac{\gamma^2L_{\mathrm{eff}}^2}{\pi\beta_2L_{\mathrm{eff,a}}}\cdot\\\mathrm{asinh}\left(\tfrac{\pi^2}{2}\beta_2L_{\mathrm{eff,a}}B_{\mathrm{ch}}^2\left[\prod_{k=1}^{\frac{N_{\mathrm{ch}}-1}{2}}\tfrac{2k\Delta f+B_{\mathrm{ch}}}{2k\Delta f-B_{\mathrm{ch}}}\right]^2\right)\end{aligned}\tag{42}$$

The product within the square brackets poses no computational problems but hinders intuition. A more compact and readable formula can be obtained, at the cost of some minor loss of accuracy (less than 0.1 dB), as follows. The product within the asinh can be approximated as:

$$\begin{aligned}&\prod_{n=1}^{\frac{N_{\mathrm{ch}}-1}{2}}\tfrac{n\Delta f+B_{\mathrm{ch}}/2}{n\Delta f-B_{\mathrm{ch}}/2}=\tfrac{\Gamma\left(1-\frac{B_{ch}}{2\Delta f}\right)}{\Gamma\left(1+\frac{B_{ch}}{2\Delta f}\right)}\cdot\tfrac{\Gamma\left(\frac{N_{ch}+1}{2}+\frac{B_{ch}}{2\Delta f}\right)}{\Gamma\left(\frac{N_{ch}+1}{2}-\frac{B_{ch}}{2\Delta f}\right)}\approx\\&\tfrac{\Gamma\left(1-\frac{B_{\mathrm{ch}}}{2\Delta f}\right)}{\Gamma\left(1+\frac{B_{\mathrm{ch}}}{2\Delta f}\right)}\left(\tfrac{N_{\mathrm{ch}}}{2}\right)^{\frac{B_{\mathrm{ch}}}{\Delta f}}\approx\left(N_{\mathrm{ch}}\right)^{\frac{B_{\mathrm{ch}}}{\Delta f}}\end{aligned}$$

where Γ is the Gamma function. The first equality above is exact. Then an approximation is found through an asymptotic formula. The final simple expression can be justified by direct numerical comparison with the preceding member, at the typical values of the parameters. Once inserted into Eq. (42), this approximation of the product yields Eq. (15).

As discussed in Sect. XI-B, the main limitation of Eq. (15) is the fact that it can be reliably used only within the restricted parameter range spelled out in Sect. XI-B itself. This loss of accuracy is mostly due to the approximation of Eq. (**??**) breaking down.

Appendix H
Derivation of Eq. (19)

The Nyquist-WDM case is addressed, at f=0. Integration is performed over the approximate square domain $\mathcal{Q}$ as discussed in App. F. Under these assumptions Eq. (19) can be rewritten as:

$$\begin{aligned}G_{\mathrm{NLI}}^{\mathrm{cc}}\left(f\right)=\tfrac{32}{27}\gamma^2G_{\mathrm{WDM}}^3L_{\mathrm{eff}}^2\sum_{n=1}^{N_s-1}\left(N_s-n\right)\cdot\\\int_{-B_{\mathrm{WDM}}/2}^{B_{\mathrm{WDM}}/2}\int_{-B_{\mathrm{WDM}}/2}^{B_{\mathrm{WDM}}/2}\tfrac{L_{\mathrm{eff}}^2}{1+16\pi^4L_{\mathrm{eff,a}}^2\beta_2^2f_1^2f_2^2}\cdot\\\cos\left(n\cdot4\pi^2\beta_2L_sf_1f_2\right)\,df_1\,df_2\end{aligned}$$

The first of the two integrals can be carried out by exploiting the following exact definite integral:

$$\begin{aligned}\int_{-q}^{q}\tfrac{b^2\cos(2n\cdot hf_1)}{b^2+h^2f_1^2}\mathrm{d}f=\tfrac{b}{h}\left[-e^{2nb}\mathrm{Im}\left\{\mathrm{Ei}\left(-2n\left[b-jhq\right]\right)\right\}-\right.\\\left.e^{-2nb}\mathrm{Im}\left\{\mathrm{Ei}\left(2n\left[b-jhq\right]\right)\right\}+\pi e^{2nb}\right]\end{aligned}$$

where Ei is the exponential-integral function, h and b are positive real numbers and n is an integer. Substituting:

$$\begin{aligned}G_{\mathrm{NLI}}^{\mathrm{cc}}\left(0\right)=\tfrac{16}{27}\gamma^2L_{\mathrm{eff}}^2\sum_{n=1}^{N_s-1}\left(N_s-n\right)\int_{-B_{\mathrm{WDM}}/2}^{B_{\mathrm{WDM}}/2}\tfrac{1}{2\pi^2\left|f_2\right|\beta_2L_{\mathrm{eff,a}}}\\\left[-e^{n\frac{L_s}{L_{\mathrm{eff,a}}}}\mathrm{Im}\left\{\mathrm{Ei}\left(-n\left[\tfrac{L_s}{L_{\mathrm{eff,a}}}-j2\pi^2\left|f_2\right|\beta_2L_sB_{\mathrm{WDM}}\right]\right)\right\}-\right.\\e^{-n\frac{L_s}{L_{\mathrm{eff,a}}}}\mathrm{Im}\left\{\mathrm{Ei}\left(n\left[\tfrac{L_s}{L_{\mathrm{eff,a}}}-j2\pi^2\left|f_2\right|\beta_2L_sB_{\mathrm{WDM}}\right]\right)\right\}+\\\left.\pi e^{n\frac{L_s}{L_{\mathrm{eff,a}}}}\right]\mathrm{d}f_2\end{aligned}$$

The second integral does not appear to have a closed-form solution. However, the overall integrand function can be approximated through a suitable sinc function, leading to the approximate formula:

$$\begin{aligned}G_{\mathrm{NLI}}^{\mathrm{cc}}\left(0\right)\approx\tfrac{16}{27}\gamma^2L_{\mathrm{eff}}^2\sum_{n=1}^{N_s-1}\left(N_s-n\right)\cdot\\\int_{-B_{\mathrm{WDM}}/2}^{B_{\mathrm{WDM}}/2}\tfrac{\sin\left(2n\pi^2\left|f_2\right|\beta_2L_sB_{\mathrm{WDM}}\right)}{n\pi^2\left|f_2\right|\beta_2L_s}\mathrm{d}f_2\end{aligned}$$

The remaining integral could then be expressed analytically through a Si (sine integral) special function. To avoid special functions, it can be observed that given the typical parameters of optical systems, the integration limits can be replaced by $\pm\infty$ without excessive errors. Resorting then to:

$$\int_{-\infty}^{\infty}\frac{\sin\left(ax\right)}{\left(ax\right)}\mathrm{d}x=\frac{\pi}{a}$$

the final result is found:

$$G_{\mathrm{NLI}}^{\mathrm{cc}}\left(0\right)\approx\frac{16}{27}\cdot\frac{\gamma^2L_{\mathrm{eff}}^2}{\pi\beta_2L_s}\cdot\sum_{n=1}^{N_s-1}\frac{\left(N_s-n\right)}{n}$$

To obtain Eq. (19) the further identity must be used:

$$\sum_{n=1}^{N_s-1}\frac{\left(N_s-n\right)}{n}=1-N_s+N_s\mathrm{HarNum}\left(N_s-1\right)$$

APPENDIX I
DERIVATION OF EQ. (24)

Under the assumption of ideal distributed amplification, the factor ρ in the GNRF is given by Eq. (10). Assuming Nyquist WDM and approximating the integration domain $\mathcal{D}$ with the square domain $\mathcal{Q}$, as shown in Fig. 24, the GNRF becomes:

$$G_{\mathrm{NLI}}(0) \approx \tfrac{16}{27}\gamma^2 G_{\mathrm{WDM}}^3 \iint\limits_{\mathcal{Q}} \left|\frac{\sin\left(2\pi^2\beta_2 f_1 f_2 L_{\mathrm{tot}}\right)}{2\pi^2\beta_2 f_1 f_2 L_{\mathrm{tot}}}\right|^2 \mathrm{d}f_1\mathrm{d}f_2$$

where L_{tot} is the total link length. The double integral can then be solved exactly, yielding:

$$G_{\mathrm{NLI}}(0) \approx \tfrac{32}{27}\gamma^2 G_{\mathrm{WDM}}^3 L_{\mathrm{tot}}^2 \cdot \Big[B_{\mathrm{WDM}}^2 \mathrm{Re}\left\{{}_3F_3\left(1,1,1;2,2,2;j\pi^2\beta_2 B_{\mathrm{WDM}}^2 L_{\mathrm{tot}}\right)\right\} + + \frac{1-\cos\left(\pi^2\beta_2 L_{\mathrm{tot}} B_{\mathrm{WDM}}^2\right)}{\pi^4\beta_2^2 L_{\mathrm{tot}}^2 B_{\mathrm{WDM}}^2} - \frac{\mathrm{Si}\left(\pi^2\beta_2 L_{\mathrm{tot}} B_{\mathrm{WDM}}^2\right)}{\pi^2\beta_2 L_{\mathrm{tot}}}\Big] \tag{43}$$

where ${}_3F_3\left(1,1,1;2,2,2;x\right)$ is a hypergeometric function, 'Re' means 'real part'and 'Si' is a sine-integral function.

This formula is highly accurate but inconvenient due to the special functions appearing in it. However, for increasing B_{WDM}, the second term in square brackets quickly goes to zero, while the third converges to the constant value $(2\pi\beta_2 L_{\mathrm{tot}})^{-1}$. Only the first term keeps growing. So, for large-enough B_{WDM}:

$$G_{\mathrm{NLI}}(0) \approx \tfrac{32}{27}\gamma^2 G_{\mathrm{WDM}}^3 L_{\mathrm{tot}}^2 \Big[B_{\mathrm{WDM}}^2 \cdot \mathrm{Re}\left\{{}_3F_3\left(1,1,1;2,2,2;j\pi^2\beta_2 B_{\mathrm{WDM}}^2 L_{\mathrm{tot}}\right)\right\} - \tfrac{1}{2\pi\beta_2 L_{\mathrm{tot}}}\Big]$$

An asymptotic form of the remaining special function is:

$$\mathrm{Re}\left\{{}_3F_3\left(1,1,1;2,2,2;jx\right)\right\} \approx \frac{\pi}{2x}\left[\log_e(x) + \gamma_e\right]$$

yielding:

$$G_{\mathrm{NLI}}(0) \approx \frac{16}{27}\gamma^2 G_{\mathrm{WDM}}^3 L_{\mathrm{tot}} \frac{\log_e\left(\pi^2\beta_2 B_{\mathrm{WDM}}^2 L_{\mathrm{tot}}\right) + \gamma_e - 1}{\pi\beta_2}$$

where γ_e is Euler's constant. The constant $(\gamma_e - 1)$ at the numerator can be brought into the log argument as $\exp(\gamma_e - 1) \approx 0.65522 \approx 2/3$ so that:

$$G_{\mathrm{NLI}}(0) \approx \frac{16}{27}\gamma^2 G_{\mathrm{WDM}}^3 L_{\mathrm{tot}} \frac{\log_e\left(\frac{2\pi^2}{3}\beta_2 B_{\mathrm{WDM}}^2 L_{\mathrm{tot}}\right)}{\pi\beta_2}$$

This formula is plotted in Fig. 19 as dashed-dotted line, showing very good accuracy, except for very low values of B_{WDM}, as expected. To avoid the non-physical behavior (negative values) for $B_{\mathrm{WDM}} \to 0$, the log function can be heuristically replaced with asinh of half the argument, finally yielding Eq. (24), whose overall accuracy is very good (Fig. 19).

Despite the similarity of Eq. (24) with Eq. (13), their respective derivations outlined in this appendix and in App. F, are very different. The apparent similarity of the end results is clearly due to similar physical processes taking place, but it stops there. Specifically, any attempt at somehow deriving the distributed amplification formula as the limit of the conventional case for $\alpha \to 0$, is certain to fail because of the approximation of the FWM efficiency term performed in Eq. (36) breaking down when loss goes to zero.

APPENDIX J
ASE NOISE FROM DISTRIBUTED AMPLIFICATION

Eq. (12), once inserted into Eq. (1), allows to estimate the NLI noise arising with backward-pumped Raman amplification. Since the final target is typically that of calculating $\mathrm{OSNR}_{\mathrm{tot}}$ as in Eq. 4, ASE noise is also necessary. In this case, the PSD of the ASE noise produced by Raman along a single span is given by [25]:

$$G_{\mathrm{ASE}} = n_{\mathrm{sp},T} \cdot h\nu \left(\tfrac{C_{\mathrm{R}}}{2\alpha_p} P_p\right)^{-\alpha/\alpha_p} e^{\frac{C_{\mathrm{R}} P_p}{2\alpha_p}} \left[\Gamma(1+\alpha/\alpha_p, \tfrac{C_R}{2\alpha_p} P_p \cdot e^{-2\alpha_p L_s}) - \Gamma(1+\alpha/\alpha_p, \tfrac{C_R}{2\alpha_p} P_p)\right] \tag{44}$$

where $n_{\mathrm{sp},T} = 1/(1-\exp(-h\Delta\nu/(k_B T))$, with h and k_B being Planck's and Boltzmann's constants, respectively, and T temperature in [K].

For the case of ideal distributed amplification, whereby $g(z) = \alpha$, then the ASE noise PSD at the end of the link is given by $G_{\mathrm{ASE}} = 4\alpha \cdot h\nu \cdot n_{\mathrm{sp},T}$

REFERENCES

[1] A. Carena, V. Curri, G. Bosco, P. Poggiolini, F. Forghieri, "Modeling of the Impact of Non-Linear Propagation Effects in Uncompensated Optical Coherent Transmission Links," *J. of Lightw. Technol.*, vol. 30, no. 10, pp. 1524-1539, May 2012.

[2] K.V. Peddanarappagari and M. Brandt-Pearce "Volterra Series Transfer Function of Single-Mode Fibers," *J. of Lightw. Technol.,* vol. 15, no. 12, pp. 2232-2241, Dec. 1997.

[3] Jau Tang, "The Channel Capacity of a Multispan DWDM System Employing Dispersive Nonlinear Optical Fibers and an Ideal Coherent Optical Receiver," *J. Lightwave Technol.,* vol. 20, no. 7, pp. 1095-1101, July 2002.

[4] Jau Tang, "A Comparison Study of the Shannon Channel Capacity of Various Nonlinear Optical Fibers," *J. Lightwave Technol.,* vol. 24, no. 5, pp. 2070-2075, May 2006.

[5] A. Splett, C. Kurzke, and K. Petermann, "Ultimate Transmission Capacity of Amplified Optical Fiber Communication Systems Taking into Account Fiber Nonlinearities," *in Proc. ECOC 1993,* vol. 2, pp. 41-44, 1993.

[6] H. Louchet et al., "Analytical Model for the Performance Evaluation of DWDM Transmission Systems," *IEEE Phot. Technol. Lett.,*, vol. 15, no. 9, pp. 1219-1221, Sept. 2003.

[7] A. Mecozzi, C. Balslev Clausen, M. Shtaif, "Analysis of Intrachannel Nonlinear Effects in Highly Dispersed Optical Pulse Transmission," *IEEE Phot. Technol. Lett.,*, vol. 12, no. 4, Apr. pp. 392-394, 2000.

[8] A. Mecozzi, C. Balslev Clausen, M. Shtaif, "System Impact of Intrachannel Nonlinear Effects in Highly Dispersed Optical Pulse Transmission," *IEEE Phot. Technol. Lett.,*, vol. 12, no. 12, pp. 1633-1635, Dec. 2000.

[9] M. Nazarathy, J. Khurgin, R. Weidenfeld, Y. Meiman, Pak Cho, R. Noe, I. Shpantzer, V. Karagodsky "Phased-Array Cancellation of Nonlinear FWM in Coherent OFDM Dispersive Multi-Span Links," *Optics Express,* vol. 16, pp. 15778-15810, 2008.

[10] X. Chen and W. Shieh, "Closed-Form Expressions for Nonlinear Transmission Performance of Densely Spaced Coherent Optical OFDM Systems," *Optics Express*, vol. 18, pp. 19039-19054, 2010.

[11] W. Shieh and X. Chen, "Information Spectral Efficiency and Launch Power Density Limits Due to Fiber Nonlinearity for Coherent Optical OFDM Systems," *IEEE Photon. Journal,* vol. 3, no. 2, pp. 158-173, Apr. 2011.

[12] P. Poggiolini, A. Carena, V. Curri, G. Bosco, F. Forghieri, "Analytical Modeling of Non-Linear Propagation in Uncompensated Optical Transmission Links," *IEEE Photon. Technol. Lett.,* vol. 23, no. 11, pp. 742-744, June 2011.

[13] A. Mecozzi, René Essiambre, "Nonlinear Shannon Limit in Pseudolinear Coherent Systems,"*J. of Lightw. Technol.*, vol. 30, no. 12, pp. 2011-2024, June 15, 2012.

[14] A. Bononi, P. Serena, N. Rossi, E. Grellier, and F. Vacondio, "Modeling Nonlinearity in Coherent Transmissions with Dominant Intrachannel-Four-Wave-Mixing," *Optics Express*, vol. 20, pp. 7777-7791, 26 March 2012.

[15] F. Vacondio, et al., "On nonlinear distortions of highly dispersive optical coherent systems," *Optics Express*, vol. 20, no. 2, Jan. 2012, pp. 1022-1032.

[16] A. Carena et al., "Statistical Characterization of PM-QPSK Signals after Propagation in Uncompensated Fiber Links", in *Proc. of ECOC 2010*, paper P4.07, Torino (Italy), Sept. 2010.

[17] E. Torrengo, et al., "Experimental Validation of an Analytical Model for Nonlinear Propagation in Uncompensated Optical Links," *Optics Express*, vol. 19, pp. 790-798, Dec. 2011.

[18] O. V. Sinkin, et al., "Scaling of Nonlinear Impairments in Dispersion-Uncompensated Long-Haul Transmission," in *Proc. of OFC 2012*, Los Angeles (US), paper OTu1A.2, Mar. 2012.

[19] G. Bosco, et. al., "Experimental Investigation of Nonlinear Interference Accumulation in Uncompensated Links," *IEEE Phot. Technol. Lett.*, vol. 24, no. 14, pp. 1230-1232, July 2012.

[20] J.F. Pina, C. Xia, A.G. Striegler and D. van den Borne, "Nonlinear tolerance of Polarization-Multiplexed QPSK transmission over mixed fiber," in *Proc. of ECOC 2011*, paper We.10.P1.63, Geneva, (CH), Sept. 2011.

[21] K. Inoue, H. Toba, "Fiber Four-Wave Mixing in Multi-Amplifier Systems with Nonuniform Chromatic Dispersion," *J. Lightwave Technol.,* vol. 13, no. 1, pp. 88-93, Jan. 1995.

[22] W. Zeiler, F. Di Pasquale, P. Bayvel, J.E. Midwinter, "Modeling of Four-Wave Mixing and Gain Peaking in Amplified WDM Optical Communication Systems and Networks," *J. Lightwave Technol.,* vol. 14, no. 9, pp. 1933-1942, Sept. 1996.

[23] G. Bosco, P. Poggiolini, A. Carena, V. Curri, and F. Forghieri, "Analytical results on channel capacity in uncompensated optical links with coherent detection," *Optics Express*, vol. 19, Dec. 2011, pp. B438-B449.

[24] G. Bosco, A. Carena, R. Cigliutti, V. Curri, P. Poggiolini, F. Forghieri, "Performance Prediction for WDM PM-QPSK Transmission over Uncompensated Links," in *Proc. OFC 2011*, paper OThO7, Los Angeles (CA), Mar. 2011.

[25] S. R. Chinn, "Analysis of Counter-Pumped Small-Signal Fibre Raman Amplifiers," *Electr. Lett.*, vol. 33, pp. 607-608, Mar. 1997.

[26] P. Poggiolini, G. Bosco, A. Carena, V. Curri, F. Forghieri, "A Detailed Analytical Derivation of the GN Model of Non-Linear Interference in Coherent Optical Transmission Systems," posted on *arXiv*, www.arxiv.org, paper identifier 1209.0394, Sept. 2012.

[27] A. Carena, P. Poggiolini, V. Curri, G. Bosco, F. Forghieri, "Evaluation of the Dependence on System Parameters of Non-Linear Interference Accumulation in Multi-Span Links," in *Proc. of ECOC 2012*, Amsterdam, paper We.2.C.6, Sept. 2012.

[28] R. Pastorelli, et al., "Investigation of the Dependence of Non-Linear Interference on the Number of WDM Channels in Coherent Optical Networks," in *Proc. of ECOC 2012*, Amsterdam, paper We.2.C.2, Sept. 2012.